



HAL
open science

Complete patient exposure during paediatric brain cancer treatment for photon and proton therapy techniques including imaging procedures

Marijke de Saint-Hubert, Guillaume Boissonnat, Uwe Schneider, Christian Bäumer, Nico Verbeek, Johannes Esser, Jörg Wulff, Florian Stuckmann, Finja Suesselbeck, Racell Nabha, et al.

► To cite this version:

Marijke de Saint-Hubert, Guillaume Boissonnat, Uwe Schneider, Christian Bäumer, Nico Verbeek, et al.. Complete patient exposure during paediatric brain cancer treatment for photon and proton therapy techniques including imaging procedures. *Frontiers in Oncology*, 2023, 13, 10.3389/fonc.2023.1222800 . hal-04258183

HAL Id: hal-04258183

<https://hal.science/hal-04258183>

Submitted on 25 Oct 2023

HAL is a multi-disciplinary open access archive for the deposit and dissemination of scientific research documents, whether they are published or not. The documents may come from teaching and research institutions in France or abroad, or from public or private research centers.

L'archive ouverte pluridisciplinaire **HAL**, est destinée au dépôt et à la diffusion de documents scientifiques de niveau recherche, publiés ou non, émanant des établissements d'enseignement et de recherche français ou étrangers, des laboratoires publics ou privés.

Complete patient exposure during paediatric brain cancer treatment for photon and proton therapy techniques including imaging procedures

Marijke De Saint-Hubert¹, Guillaume Boissonnat², Uwe Schneider³, Christian Bäumer⁴, Nico Verbeek⁴, Johannes Esser⁴, Jörg Wulff⁴, Florian Stuckmann⁴, Finja Suesselbeck⁴, Raccel Nabha¹, Jérémie Dabin¹, Fabiano Vasi³, Stephan Radonic³, Miguel Rodriguez⁵, Anne C. Simon², Neige Journy⁶, Beate Timmermann⁷, Isabelle Thierry-Chef⁸, Lorenzo Brualla^{4*}

¹Belgian Nuclear Research Centre (SCK CEN), Belgium, ²Commissariat à l'Energie Atomique et aux Energies Alternatives (CEA), France, ³University of Zurich, Switzerland, ⁴West German Proton Therapy Centre Essen (WPE), Germany, ⁵Hospital Paitilla, Panama, ⁶Institut National de la Santé et de la Recherche Médicale (INSERM), France, ⁷Clinic for Particle Therapy, Essen University Hospital, Germany, ⁸Instituto Salud Global Barcelona (ISGlobal), Spain

Submitted to Journal:
Frontiers in Oncology

Specialty Section:
Radiation Oncology

Article type:
Original Research Article

Manuscript ID:
1222800

Received on:
15 May 2023

Revised on:
07 Aug 2023

Journal website link:
www.frontiersin.org

Conflict of interest statement

The authors declare that the research was conducted in the absence of any commercial or financial relationships that could be construed as a potential conflict of interest

Author contribution statement

MD: dose and risk calculations, data analysis, writing. GB: imaging dose simulations, writing. US: treatment-planning, risk calculations, data analysis, writing. CB: treatment planning, imaging protocols, writing-review. NV: proton simulations, writing-reviewing. JE: Monte Carlo geometry coding. JW: proton simulations. FS: photon simulations. FS: photon simulations and data analysis. NR: data analysis. JD: methodology, writing-review. FV: data analysis. SR: data analysis. MR: photon simulations, data processing. ACS: CT scanner geometry, NJ: epidemiological analysis, writing-review. BT: clinical analysis, writing-review. ITC: project coordinator, writing-review. LB: Monte Carlo simulations, conceptualization, supervision, writing, writing-review, editing. All authors contributed to the article and approved the submitted version.

Keywords

Photon radiotherapy, Proton therapy, Out-of-field dosimetry, imaging dosimetry, Monte Carlo simulation, Secondary cancer risk

Abstract

Word count: 311

Background: In radiotherapy, especially when treating children, minimising exposure of healthy tissue can prevent the development of adverse outcomes, including second cancers. In this study we propose a validated Monte Carlo framework to evaluate the complete patient exposure during paediatric brain cancer treatment.

Materials and methods: Organ doses were calculated for treatment of a diffuse midline glioma (50.4 Gy with 1.8 Gy per fraction) on a 5-year-old anthropomorphic phantom with 3D-conformal radiotherapy, intensity modulated radiotherapy (IMRT), volumetric modulated arc therapy (VMAT) and intensity modulated pencil beam scanning (PBS) proton therapy. Doses from computed tomography (CT) for planning and on-board imaging for positioning (kV-cone beam CT and X-ray imaging) accounted for the estimate of the exposure of the patient including imaging therapeutic dose. For dose calculations we used validated Monte Carlo-based tools (PRIMO, TOPAS, PENELOPE), while lifetime attributable risk (LAR) was estimated from dose-response relationships for cancer induction, proposed by Schneider et al.

Results: Out-of-field organ dose equivalent data of proton therapy are lower, with doses between 0.6 mSv (testes) and 120 mSv (thyroid), when compared to photon therapy revealing the highest out-of-field doses for IMRT ranging between 43 mSv (testes) and 575 mSv (thyroid). Dose delivered by CT ranged between 0.01 mSv (testes) and 72 mSv (scapula) while a single imaging positioning ranged between 2 μ Sv (testes) and 1.3 mSv (thyroid) for CBCT and 0.03 μ Sv (testes) and 48 μ Sv (scapula) for X-ray. Adding imaging dose from CT and daily CBCT to the therapeutic demonstrated an important contribution of imaging to the overall radiation burden in the course of treatment, which is subsequently used to predict the LAR, for selected organs.

Conclusion: The complete patient exposure during paediatric brain cancer treatment was estimated by combining the results from different Monte Carlo-based dosimetry tools, showing that proton therapy allows significant reduction of the out-of-field doses and secondary cancer risk in selected organs.

Contribution to the field

The use of radiation to treat cancer has evolved into modern high-precision techniques, such as intensity-modulated radiotherapy, volumetric modulated arc therapy and pencil beam scanning proton therapy. Although radiotherapy saves lives, stray radiation affects healthy tissue close and far from the treated volume. Furthermore, the introduction of intensive imaging procedures, aimed at a higher treatment precision, can add a significant dose to the patient. In the case of children, the balance between benefits and risks in the medical use of ionizing radiation has even a higher priority. Unfortunately, up until now, no research has been conducted on the complete out-of-field patient exposure, that is, taking also into account the therapeutic imaging dose. This work proposes an all-inclusive framework of different dosimetry tools that enables to get insight into the entire stray radiation exposure during paediatric brain cancer treatment. Photon and proton radiotherapy techniques are compared and the contribution of various imaging procedures, such as planning computed tomography and X-ray on-board imaging, are considered. Results suggest that proton therapy can considerably reduce healthy tissue dose and adverse outcomes, including secondary cancers. Concurrently, imaging dose as part of the radiotherapy treatment should be evaluated in a more balanced manner.

Ethics statements

Studies involving animal subjects

Generated Statement: No animal studies are presented in this manuscript.

Studies involving human subjects

Generated Statement: No human studies are presented in the manuscript.

Inclusion of identifiable human data

Generated Statement: No potentially identifiable images or data are presented in this study.

Data availability statement

Generated Statement: The raw data supporting the conclusions of this article will be made available by the authors, without undue reservation.

In review

Complete patient exposure during paediatric brain cancer treatment for photon and proton therapy techniques including imaging procedures

Marijke De Saint-Hubert¹, Guillaume Boissonnat², Uwe Schneider³, Christian Bäumer^{4,5,6,7}, Nico Verbeek^{4,5}, Johannes Esser^{4,5,8}, Jörg Wulff^{4,5}, Florian Stuckmann^{4,5}, Finja Suesselbeck^{4,5}, Racell Nabha¹, Jérémie Dabin¹, Fabiano Vasi³, Stephan Radonic³, Miguel Rodriguez^{9,10}, Anne Catherine Simon², Neige Journy¹¹, Beate Timmermann^{4,5,6,12,13}, Isabelle Thierry-Chef^{14,15,16}, Lorenzo Brualla^{4,5,6,12,*}

¹Belgian Nuclear Research Center (SCK CEN), Mol, Belgium

²CEA, Université Paris-Saclay, Palaiseau, France

³Physik Institut, Universität Zürich, Zürich, Switzerland

⁴West German Proton Therapy Centre Essen WPE, Essen, Germany

⁵West German Cancer Centre (WTZ), Essen, Germany

⁶Radiation Oncology and Imaging, German Cancer Consortium DKTK, Essen, Germany

⁷Department of Physics, TU Dortmund University, Dortmund, Germany

⁸Faculty of Mathematics and Science Institute of Physics and Medical Physics, Heinrich-Heine University, Düsseldorf, Germany

⁹Hospital Paitilla, Panama City, Panama

¹⁰Instituto de Investigaciones Científicas y de Alta Tecnología INDICASAT-AIP, Panama City, Panama

¹¹INSERM U1018, Paris Sud-Paris Saclay University, Villejuif, France

¹²Faculty of Medicine, University of Duisburg-Essen, Essen, Germany

¹³Department of Particle Therapy, University Hospital Essen, Germany

¹⁴Barcelona Institute of Global Health (ISGlobal), Barcelona, Spain

¹⁵University Pompeu Fabra, Barcelona, Spain

¹⁶CIBER Epidemiología y Salud Pública, Madrid, Spain

Correspondence*:

Lorenzo Brualla

Lorenzo.Brualla@uni-due.de

2 ABSTRACT

3 **Background:** In radiotherapy, especially when treating children, minimising exposure of healthy
4 tissue can prevent the development of adverse outcomes, including second cancers. In this study
5 we propose a validated Monte Carlo framework to evaluate the complete patient exposure during
6 paediatric brain cancer treatment.

7 **Materials and methods:** Organ doses were calculated for treatment of a diffuse midline glioma
8 (50.4 Gy with 1.8 Gy per fraction) on a 5-year-old anthropomorphic phantom with 3D-conformal
9 radiotherapy, intensity modulated radiotherapy (IMRT), volumetric modulated arc therapy (VMAT)
10 and intensity modulated pencil beam scanning (PBS) proton therapy. Doses from computed
11 tomography (CT) for planning and on-board imaging for positioning (kV-cone beam CT and
12 X-ray imaging) accounted for the estimate of the exposure of the patient including imaging
13 therapeutic dose. For dose calculations we used validated Monte Carlo-based tools (PRIMO,
14 TOPAS, PENELOPE), while lifetime attributable risk (LAR) was estimated from dose-response
15 relationships for cancer induction, proposed by Schneider et al.

16 **Results:** Out-of-field organ dose equivalent data of proton therapy are lower, with doses between
17 0.6 mSv (testes) and 120 mSv (thyroid), when compared to photon therapy revealing the highest
18 out-of-field doses for IMRT ranging between 43 mSv (testes) and 575 mSv (thyroid). Dose
19 delivered by CT ranged between 0.01 mSv (testes) and 72 mSv (scapula) while a single imaging
20 positioning ranged between 2 μ Sv (testes) and 1.3 mSv (thyroid) for CBCT and 0.03 μ Sv (testes)
21 and 48 μ Sv (scapula) for X-ray. Adding imaging dose from CT and daily CBCT to the therapeutic
22 demonstrated an important contribution of imaging to the overall radiation burden in the course of
23 treatment, which is subsequently used to predict the LAR, for selected organs.

24 **Conclusion:** The complete patient exposure during paediatric brain cancer treatment was
25 estimated by combining the results from different Monte Carlo-based dosimetry tools, showing
26 that proton therapy allows significant reduction of the out-of-field doses and secondary cancer
27 risk in selected organs.

28 **Keywords:** photon radiotherapy, proton therapy, out-of-field dosimetry, imaging dosimetry, Monte Carlo simulation, secondary cancer
29 risk

1 HIGHLIGHTS

- 30 • Complete patient exposure during paediatric brain cancer treatment is estimated by combining different
31 dosimetry tools.
- 32 • Imaging dose significantly contributes to the out-of-field doses in proton therapy while its contribution
33 is proportionally much lower for photon treatments.
- 34 • Proton therapy allows to considerably decrease the out-of-field doses and thus risk of secondary cancer
35 when compared to photon therapy.

2 INTRODUCTION

36 Improvements of radiotherapy procedures have had a major impact on survival of paediatric patients. While
37 benefits to the patient largely outweigh risks associated with the therapeutic use of ionising radiation,
38 the late effects of exposure are particularly important to understand for children with high probability of
39 tumour control.

40 Recent large cohort studies of children exposed to low doses from computerised tomography (CT) scans
41 have shown increased risks of leukaemia and brain tumours (Pearce et al., 2012; Mathews et al., 2013;
42 Journy et al., 2019; Huang et al., 2014; Pokora et al., 2016). Very recently, the results of the EPI-CT study,
43 i.e. the European project on radiation-related risk of cancer in a large multinational cohort of more than one
44 million paediatric patients involved in CT scanning, reported on a significant dose-response relationship

45 between CT-related radiation exposure and brain cancer and emphasised careful justification of paediatric
46 CTs and use of doses as low as reasonably possible (Hauptmann et al., 2023). Large-scale follow-up
47 of childhood cancer survivors has been performed for patients exposed before 2000 and for exposures
48 to older techniques, such as 2D and early 3D conformal radiotherapy techniques (Constine et al., 2019;
49 Wang et al., 2022; Palmer et al., 2021). A more recent epidemiological study on the risk of a secondary
50 cancer diagnosis showed to be similar after intensity-modulated radiotherapy (IMRT) versus 3D-conformal
51 radiotherapy (3D-CRT), whereas proton therapy pencil beam scanning (PBS) was associated with a lower
52 risk of secondary cancer (Xiang et al., 2020). However, some epidemiological studies have failed to provide
53 convincing evidence of the lower risk associated to proton therapy with respect to photon therapy, mainly
54 due to small sample sizes (particularly for paediatric patients), too short follow-up times (less than 10
55 years for the majority of patients), and potential selection (e.g. indication, follow-up) and confounding (e.g.
56 insufficient information on chemotherapy) biases (Weber et al., 2018; Chung et al., 2013).

57 In this context, the HARMONIC project (HARMONIC, 2019; Harbron et al., 2020) aims at
58 complementing these recent studies by improving the understanding of the health effects of medical
59 ionising radiation exposure of paediatric patients. This HORIZON 2020 European Commission project,
60 not only addresses the issues on secondary cancer risk, but also risks associated with other late outcomes
61 (including endocrine dysfunctions, cardio- and neurovascular damages, and patient/parent-reported quality
62 of life, fatigue and educational outcomes) and the construction of the necessary infrastructure for their
63 future study.

64 Paediatric patients undergoing radiotherapy are exposed to ionising radiation, as a consequence of
65 the treatment, but also from complementing imaging procedures. Experimental dosimetry studies have
66 been performed extensively within the European Radiation Dosimetry Group (EURADOS) WG9, using
67 paediatric anthropomorphic phantoms during photon therapy (Majer et al., 2017; De Saint-Hubert et al.,
68 2018, 2017) and more recently during proton therapy (Knežević et al., 2018; Majer et al., 2022; Wochnik
69 et al., 2021). Furthermore, Athar et al. (2010) simulated out-of-field doses for an 8-year phantom and for
70 different 6-MV IMRT plans and compared with passive and active proton therapy techniques (Athar et al.,
71 2010). However, only rarely were data complemented with doses from imaging (De Saint-Hubert et al.,
72 2017; Gudowska et al., 2014).

73 Until now, the imaging dose during radiotherapy was generally considered negligible in clinical practice
74 because of its low magnitude compared to the therapeutic dose given at the treated volume. Nevertheless,
75 the use of on-board imaging (OBI) for accurate patient positioning has become even more frequent for
76 advanced radiotherapy, such as proton therapy. Therefore, sufficient attention should be given to the dose
77 delivered to the patient by imaging procedures. Moreover, doses from therapeutic exposures should be
78 complemented with imaging doses to have a complete picture of the absorbed dose distribution.

79 Within HARMONIC, a tool for calculating the dose from imaging procedures during radiotherapy has
80 been further developed (Boissonnat et al., 2020). Furthermore, HARMONIC has invested substantial
81 efforts into validating computational and analytical tools needed to estimate out-of-field organ doses in
82 children treated with photon and proton therapy (De Saint-Hubert et al., 2022a,b). Particularly important
83 for proton therapy are the challenges related to the creation of secondary neutrons and the higher relative
84 biological effectiveness (RBE) of neutrons and protons when compared to photons. Previous work shows
85 the presence of different radiation types in this mixed field of stray radiation in proton therapy including
86 variable RBE (De Saint-Hubert et al., 2022b; Domingo et al., 2022). We believe that it is essential to
87 combine doses from different procedures in order to make a valid comparison between proton and photon
88 radiotherapy.

89 Previous studies have used the absorbed dose (Yeom et al., 2022, 2020) or have applied an average quality
90 factor for neutrons to consider the RBE of neutrons (Kalbasi et al., 2018).

91 A Monte Carlo study on fetal dose during brain radiotherapy considered the biological effects of neutrons
92 by estimating the quality factor provided in ICRP Publication 60 (ICRP 1991) for proton therapy. This
93 enabled a fair comparison between proton and photon therapy demonstrating a 10-fold reduction in the
94 fetal dose between PBS proton therapy, and 3D-CRT (Geng et al., 2015). Others have focused only on
95 neutron dose equivalent and, as such, have neglected the contributions from protons close to the field and
96 gamma contributions to the out-of-field doses (Athar et al., 2010), while others have taken care of the
97 neutron contribution to the out-of-field dose in high energy photon treatments (Sánchez-Nieto et al., 2018).
98 Interestingly, a recent and unique study on measurements of secondary radiation doses in child brain cancer
99 has allowed to compare proton therapy with photon therapy (3D-CRT, IMRT and GammaKnife) (Knežević
100 et al., 2022). Our study is complementary to the study from Knežević et al., but expands to cover the
101 complete patient exposure during paediatric brain cancer treatment, including imaging. Moreover, we
102 projected potential subsequent lifetime risks of secondary cancers following paediatric brain radiotherapy,
103 according to a semi-mechanistic risk model proposed by Schneider et al. (2011).

3 MATERIAL AND METHODS

104 3.1 Brain cancer radiotherapy techniques

105 Aiming to simulate a realistic treatment of a brain tumour, a clinically applied treatment plan was
106 transferred to the conditions of the experiment. A 7-year-old female patient was selected with a diffuse
107 midline glioma (WHO grade IV). The patient received a combined radiotherapy and chemotherapy after
108 R3 resection. The concerned patient was enrolled in the prospective registry study ‘KiProReg’ (German
109 Clinical Trials Register: DRKS-ID: DRKS00005363) after consent from her legal guardians. This study
110 was approved by the local ethics committee.

111 The clinical proton plan was transferred to an anthropomorphic phantom (ATOM, Computerized
112 Imaging Reference Systems (CIRS), Inc.) representing a 5-year-old child (type 705D). A median dose of
113 $D_{\text{prescribed}} = 50.4 \text{ Gy(RBE)}$ with 1.8 Gy(RBE) per fraction was prescribed to the initial planning target
114 volume (PTV), which was located in the cerebellum and had a volume of 195.2 cm^3 . The proton treatment
115 plan consisted of two ipsilateral oblique fields and a contralateral oblique field (see figure 1). The proton
116 fields were delivered in a gantry room in PBS delivery mode employing a lucite range shifter with a
117 thickness of 4.44 cm and a water-equivalent thickness of 5.14 cm. The treatment planning of the phantom
118 case was conducted as described previously (De Saint-Hubert et al., 2022b).

119 For comparison, the anthropomorphic phantom was treated with photon therapy featuring the same
120 cranial size and shape. Three techniques were applied, namely 3D-CRT, IMRT and volumetric modulated
121 arc therapy (VMAT). All photon irradiations for this study were done with a Varian TrueBeam STx LINAC
122 operating with a flattening filter at a nominal energy of 6 MV. The linac was equipped with a Varian
123 Millennium 120 multileaf collimator. The same dose of 50.4 Gy with 1.8 Gy per fraction was prescribed
124 to the initial PTV. The 3D-CRT plan used two lateral fields with beam angles 90° and 270° . The IMRT
125 plan consisted of five coplanar and isocentric fields with beam angles of 70° , 125° , 180° , 235° and 280° ,
126 respectively. VMAT was planned using two 360° isocentric rotations. The plans were optimised with the
127 photon optimisation algorithm PO (Varian Medical Systems, Version 13.6). The plans were iteratively
128 optimised over several steps using the constraint $V7\text{Gy}=4\%$ for the eye and $V40\text{Gy}=5\%$ and $V25\text{Gy}=5\%$,

129 for the left and right cochlea respectively, and $V98\%[PTV]>95\%$ regarding $D_{\text{prescribed}}$. More details can
 130 be found in a recently published paper (De Saint-Hubert et al., 2022a).

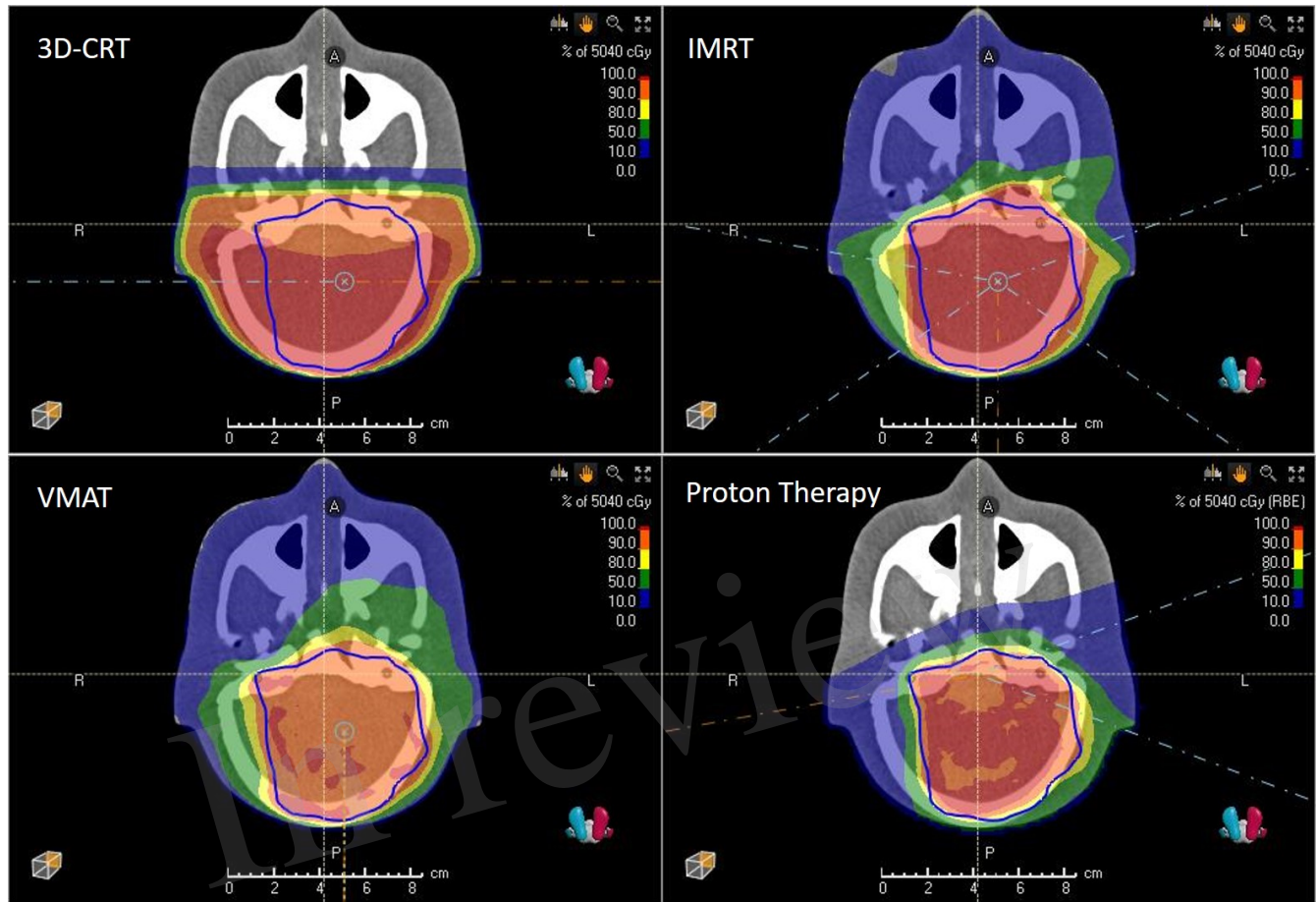


Figure 1. 3D-CRT, IMRT, VMAT and PBS proton therapy plans showing isodoses and PTV (blue) as computed by the treatment planning system.

131 **3.2 Imaging during brain cancer treatment**

132 In order to evaluate doses delivered by X-ray based imaging systems during the course of either proton
 133 or photon therapy, Monte Carlo simulations computed the imaging absorbed dose distributions on the
 134 paediatric anthropomorphic phantom for all imaging exams that the actual treatment would have required,
 135 namely the CT exam used for planning and the OBI exams used for positioning during treatment. In
 136 practice, the proton therapy centre uses daily X-ray imaging protocol while the photon therapy centre uses
 137 daily kV-CBCT (kilo-voltage cone beam computed tomography) protocol for all radiotherapy techniques.

138 **3.2.1 Computed Tomography**

139 For planning exams, CT protocols vary very little within the same treatment centre. Nevertheless, the
 140 scan length and the X-ray tube current are often dependent on the patient morphology and pathology.
 141 Thus, we used as reference protocol the one actually delivered to the paediatric patient treated at the West
 142 German Proton Therapy Centre Essen (WPE) on its Philips Big Bore CT scanner (Philips HealthCare, The
 143 Netherlands): 120 kVp, single fixed filter, 12 mm collimation, 210 mA, 287 mm of scan length and an
 144 exposure time of 31.9 s.

145 3.2.2 kV-CBCT

146 To depict the daily OBI exams performed during a radiotherapy treatment on a TrueBeam (Varian) we
 147 selected the kV-CBCT ‘head low dose’ protocol. It corresponds to an irradiation on a partial anteroposterior
 148 arc of 200° performed at 100 kVp, with the full-fan filter (with titanium foil, bowtie shaped) and 146 mA s
 149 (20 mA and 20 ms per projection and 364 projections), using 22.2 cm × 16.6 cm field size at source-axis
 150 distance (SAD). This exam is repeated at each treatment session and for the studied clinical case this
 151 corresponds to 28 times (Schneider et al., 2015).

152 3.2.3 X-ray based patient positioning and verification system

153 To portray the daily OBI practice, we used the WPE X-ray protocol optimised for position verification
 154 of tumours with localisation in the head of children with the proton gantry positioned at 0°. It consists
 155 of making a first image using the X-ray tube A, on the same direction as the treatment beam at 90 kVp,
 156 12 mA and 100 ms (SAD of 1511 mm, field size of 20.2 cm × 27.9 cm); as well as a second image with
 157 X-ray tube B, oriented at 270° from the treatment beam direction at 90 kVp, 32 mA and 100 ms (SAD of
 158 2870 mm, field size of 24.4 cm × 33.8 cm). This exam is repeated at each treatment session and for the
 159 studied clinical case, this corresponds to 28 times.

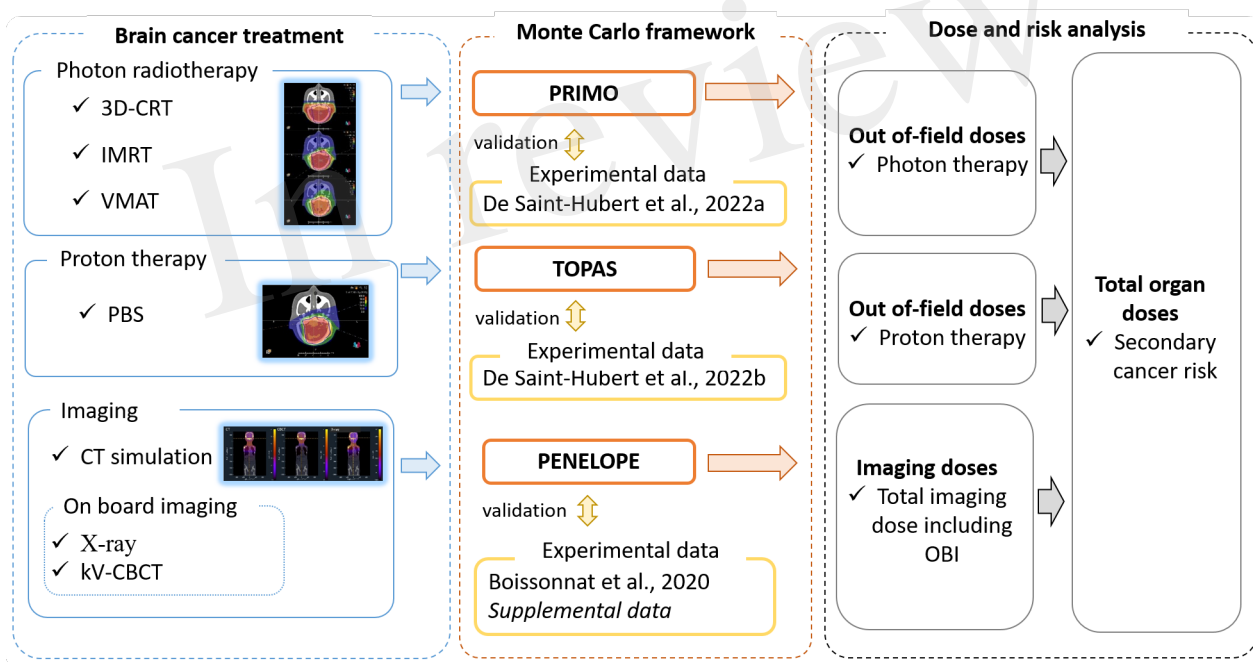


Figure 2. Schematic overview of the study design. Brain cancer treatment plan, involving different radiotherapy techniques and imaging protocols, were used as input to a Monte Carlo framework. This framework was validated with experimental data and provided out-of-field radiotherapy and imaging doses which were combined to derive estimates of total organ doses and secondary cancer risks.

160 3.3 Monte Carlo framework

161 The whole-body absorbed dose distributions presented have all been computed with general-purpose
 162 radiation transport Monte Carlo codes. In all cases, the DICOM-CT image of the anthropomorphic 5-year-
 163 old CIRS phantom was used for the Monte Carlo radiation transport. The validations of these simulations
 164 were done by comparison of the Monte Carlo-computed doses with the experimental values obtained by

165 detectors, such as thermoluminescent detectors (TLDs) and bubble detectors, inserted in the CIRS phantom.
166 These validations have been already published, as well as the detailed description of the simulations and
167 experiments (De Saint-Hubert et al., 2022a,b). Figure 2 shows the Monte Carlo framework used to calculate
168 the doses from radiotherapy and imaging procedures. The Monte Carlo codes that have been used and the
169 corresponding simulations are presented below.

170 3.3.1 PRIMO simulations for out-of-field photon doses

171 PRIMO (version 1.0.64.1814) (Rodriguez et al., 2013, 2012), a Monte Carlo dose verification system
172 that simulates medical linacs and computes the subsequent absorbed dose, was used to calculate out-
173 of-field doses in the cases of photon radiotherapy. PRIMO uses penEasy/PENELOPE (Sempau et al.,
174 2011; Baró et al., 1995; Sempau et al., 1997) for the simulation of the radiation transport starting from
175 the primary electron beam exiting the bending magnet, through the actual geometrical description of
176 the linac, downstream to the collimating jaws. At that position, a phase-space was tallied, which was
177 subsequently used as radiation source for simulating the 3D-CRT, IMRT and VMAT treatments (Rodriguez
178 et al., 2015). PRIMO used the fast Monte Carlo code DPM (Sempau et al., 2000; Rodriguez and Brualla,
179 2018; Rodriguez et al., 2018) for the simulations of these treatments and tallied the corresponding absorbed
180 dose distributions in the CT image of the CIRS phantom. Calculated absorbed doses were converted to
181 dose equivalent considering an RBE= \neq /Q-factor=1. More information can be found in (De Saint-Hubert
182 et al., 2022a).

183 3.3.2 TOPAS simulations for out-of-field proton doses

184 The Geant4 (Agostinelli et al., 2003; Allison et al., 2006, 2016) wrap-up code TOPAS v3.6 (Geant4) (Perl
185 et al., 2012), in conjunction with the Matlab-based (The Mathworks, Inc. Natick, Massachusetts) dose
186 verification system matRad v2.10.1 (Wieser et al., 2017), were used to simulate the out-of-field absorbed
187 dose distribution in the case of the PBS proton therapy of the CIRS phantom. For this purpose, matRad was
188 extended by including the possibility to process DICOM RTIon files. Thanks to this feature it was possible
189 to create the TOPAS input files with the treatment room-specific radiation parameters. The simulations
190 for the determination of the neutron dose equivalent at a point and the proton and gamma out-of-field
191 dose could then be conducted. Following a validation of the Monte Carlo framework, TOPAS simulations
192 were used to compute the total dose equivalent. Details of the experiments and simulations are given
193 in (De Saint-Hubert et al., 2022b).

194 3.3.3 PENELOPE-based tool for imaging doses

195 The Monte Carlo framework for computing imaging absorbed doses is based on an in-house modified
196 version of PENELOPE 2006 that introduced parallelisation and the possibility to use voxelised geometries
197 (previously described in (Boissonnat et al., 2020)). Calculated absorbed doses were converted to dose
198 equivalent considering an RBE= \neq /Q-factor=1. This version of PENELOPE has been used previously in a
199 software prototype dedicated to OBI dosimetry estimation as part of the Additional Imaging Doses—Image
200 Guided Radiation Therapy project (ANR-15-CE19-0009) (Le Deroff et al., 2022). This software already
201 included a model of the OBI imaging system used on the TrueBeam linac and was expanded to include
202 both the stereo imaging system used at the WPE proton beam lines and the Philips Big Bore CT scanner.
203 Experimental Monte Carlo model validation for both systems are presented in annex 1.

204 3.4 Calculation of dose equivalent per organ

205 The CIRS phantom contains 180 organ-specific inserts and allowed to estimate the dose equivalent for 22
 206 organs by averaging the calculated data from organ-specific locations. For radiotherapy we calculated the
 207 dose equivalent per organ considering a total target dose of 50.4 Gy(RBE). For proton therapy, an RBE of
 208 1.1 was considered and an absorbed dose of 45.8 Gy was used for the normalization of out-of-field organ
 209 dose. For photon therapy the total absorbed target dose was 50.4 Gy. For imaging, the dose equivalent per
 210 organ was calculated from a single imaging procedure for CT, kV-CBCT and X-ray. Then, we summed
 211 the dose equivalent per organ for the different imaging procedures by assuming the following: i) a single
 212 planning CT scan (1*CT) and, ii) a daily OBI (28*kV-CBCT or 28*X-ray). Finally, to get an estimate
 213 of the total dose equivalent per organ, during the entire radiotherapy treatment, the dose equivalent from
 214 radiotherapy and imaging was summed for each organ.

215 In the plots that follow, the error bars represent the spread on the calculated average dose equivalent per
 216 organ and not the uncertainties. The number of points in an organ varies among organs as described by the
 217 manufacturer (CIRS, 2013). Standard statistical uncertainties of the Monte Carlo calculations are described
 218 in previous papers (De Saint-Hubert et al., 2022a,b), reporting up to 31% for TOPAS while for the PRIMO
 219 calculations of 3D-CRT, IMRT and VMAT the uncertainty was on average 11%. The standard statistical
 220 uncertainties of Monte Carlo calculations of the imaging procedures were on average 20%, 27%, and 16%
 221 for CT, CBCT and X-ray, respectively.

222 3.5 Lifetime attributable risk for secondary cancer

223 In this study we applied the carcinogenesis model, previously published (Schneider et al., 2011), to
 224 estimate secondary cancer risk which emphasises cell kinetics of radiation-induced cancer by mutational
 225 processes and applies to advanced radiotherapy techniques as well as imaging dose. Briefly, the model
 226 describes carcinoma induction after fractionated radiotherapy as an analytical function and integrates
 227 cell sterilisation processes described by the linear-quadratic model and repopulation effects. The linear-
 228 quadratic model of cell kill is applied to normal tissues that are irradiated during radiotherapy. Tumour
 229 induction is modelled such that each transformation process results in a tumour cell. Cancer induction in
 230 this model is a function of treatment dose, dose per fraction, defined cell kill parameters, tumour induction
 231 variable and the repopulation parameter. The obtained dose-response relationship for carcinoma induction
 232 can be used to calculate excess absolute risk (EAR):

$$233 \text{EAR}(a) = \beta(\text{EAR}) \mu(e, a) \left[\frac{\exp(-\alpha' D)}{\alpha' R} \right] \left[1 - 2R + R^2 \exp(\alpha' D) - (1 - R)^2 \exp\left(-\frac{\alpha' R}{1 - R} D\right) \right]. \quad (1)$$

234 The model parameters were used from the publication of Schneider et al., as obtained by fits to several
 235 epidemiological, cancer specific carcinogenesis data for carcinoma induction (Schneider et al., 2011). By
 236 applying these parameters the radiation induced cancer estimates were determined. Here, D is the average
 237 dose equivalent, at the respective organ location, as computed within our study (units mSv) and $\beta(\text{EAR})$
 238 is referring to the initial slope, which is the slope of the dose-response curve at low dose for each site.
 239 These are tabulated in table 1 of Schneider et al. (2011) for a Western population. The repopulation/repair
 240 parameter R characterises the repopulation/repair-ability of the tissue between two dose fractions and is
 241 0 if no and 1 if full repopulation/repair occurs. Moreover, α' is the cell kill parameter for fractionated
 treatment as defined by:

$$\alpha' = \alpha + \beta \frac{D}{D_t} d_t, \quad (2)$$

242 where D_t and d_t is the prescribed dose to the target volume with the corresponding fractionation dose,
 243 respectively. It is assumed here an $\alpha/\beta = 3$ Gy for all tissues.

244 The function $\mu(e, a)$ in equation 1 describes the age variation of EAR and depends on the age of exposure
 245 e and the attained age a in years:

$$\mu(e, a) = \exp \left[\gamma_e (e - 30) + \gamma_a \ln \left(\frac{a}{70} \right) \right]. \quad (3)$$

246 The age modifying parameters γ_e and γ_a for a Japanese population and for different sites are taken from
 247 table 1 in Schneider et al. (2011). In this form the fit parameters are sex-averaged and centred at an age at
 248 exposure of 30 years and an attained age of 70 years. For the calculations in the present work the age of
 249 exposure was 5 years. The formulation of EAR as defined by equation 1 gives the risk of secondary cancer
 250 induction at an attained age a . However, it is more convenient to estimate a lifetime attributable risk (LAR)
 251 for the patient, which is the EAR integrated from $a = e$ to the life expectancy a_{\max} . The determination of
 252 LAR was done as described by Kellerer et al. (2001):

$$\text{LAR} = \sum_e^{a_{\max}} \text{EAR}(a) \frac{S(a)}{S(e)}, \quad (4)$$

253 where the survival function $S(a)$ (taken from Kellerer et al. (2001)) is the probability at birth to reach
 254 at least age a , while $S(e)$ is the probability to be alive at the age of exposure. Thus $S(a)/S(e)$ is the
 255 conditional probability of a person to be alive at age e and reach age a . LAR is calculated by summing
 256 between $e = 5$ and $a_{\max} = 90$ years for six organs susceptible for secondary solid tumour induction,
 257 namely bladder, breast, liver, lung, stomach and thyroid.

4 RESULTS

258 4.1 Out-of-field dose equivalent per organ during radiotherapy

259 In Figure 3 the out-of-field dose equivalent per organ is plotted for various photon radiotherapy techniques
 260 (3D-CRT, IMRT and VMAT) and PBS proton therapy. Within the photon radiotherapy techniques the
 261 dose equivalent in thyroid ranges between 500 mSv and 620 mSv for VMAT and 3D-CRT, respectively. In
 262 breast, the dose equivalent is most pronounced for IMRT, 290 mSv, as compared to 160 mSv and 190 mSv
 263 for 3D-CRT and VMAT, respectively. For organs in the thorax region, such as lungs and heart, the dose
 264 equivalent is more comparable between the different photon techniques. Still VMAT irradiation resulted in
 265 lower average lung and heart dose equivalent of 160 mSv and 130 mSv. The further away from the target,
 266 the more visible is the decreased out-of-field dose equivalent for VMAT, when compared to IMRT which
 267 yields the highest out-of-field dose equivalent.

268 The out-of-field dose equivalent during proton therapy is in all cases lower than photon therapy techniques
 269 and ranges from 120 mSv in thyroid down to 0.6 mSv in testes. The difference to photon techniques becomes
 270 larger, the further away from the target. For example, the out-of-field dose equivalent ratio between IMRT
 271 and proton therapy ranges from 4.8 in thyroid up to 74 in testes.

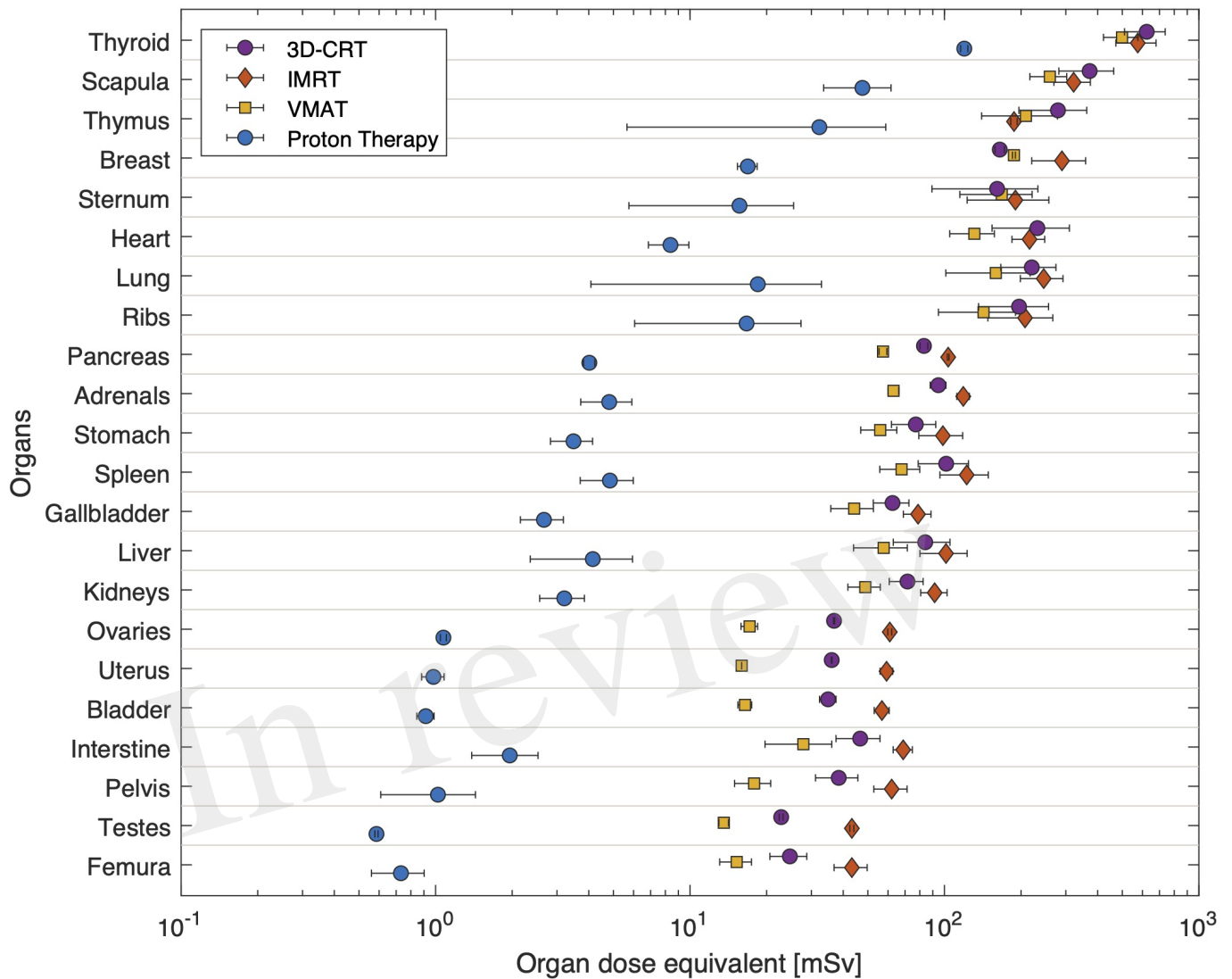


Figure 3. Average dose equivalent per organ from radiotherapy for different techniques, 3D-CRT, IMRT, VMAT and PBS proton therapy. Organs are sorted according to their distance to target. Horizontal bars correspond to the spread of doses as calculated at various locations inside the organ.

272 **4.2 Out-of-field dose equivalent per organ from imaging**

273 Doses during imaging procedures were calculated using Monte Carlo-based software. Figure 4 shows
 274 the dose equivalent distributions (mSv) projected on the central coronal plane of the the 5-year-old CIRS
 275 phantom CT. It should be noted that the colourbar scale in that figure is relative to the respective maximum
 276 of each modality, namely for CT 0-70 mSv, for CBCT 0-12 mSv and for X-ray 0-70 μ Sv.

277 In figure 5 the dose equivalent per organ is shown as computed for a single imaging procedure. It is
 278 clear that CT results in elevated dose equivalent per organ when compared to OBI techniques such as
 279 kV-CBTC and X-ray. CT doses range between 0.01 mSv (testes) and 72 mSv (scapula) while for CBCT this
 280 is between 0.5 μ Sv (testes) and 1.3 mSv (thyroid). For X-ray the dose equivalent ranges between 0.02 μ Sv

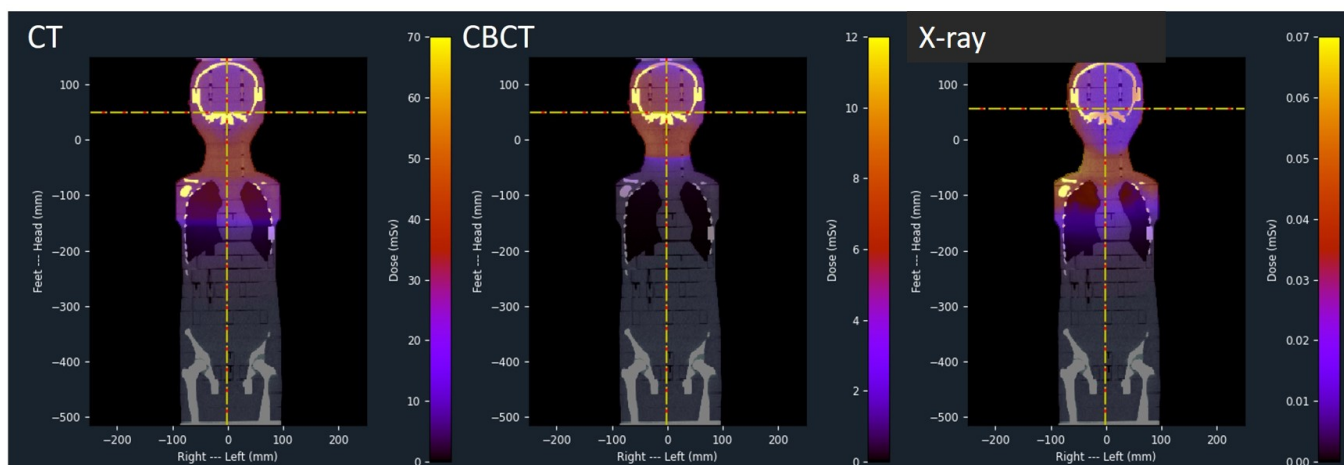


Figure 4. Dose equivalent distributions of CT, kV-CBCT and X-ray as projected on the central coronal plane of the 5-year-old CIRS phantom.

281 (testes) and $56 \mu\text{Sv}$ (scapula). Organs in the thorax region spreading over long distances in the coronal
 282 plane, such as sternum, ribs and lungs, demonstrate large spread of computed dose equivalent, indicating a
 283 large dose gradient.

284 When considering a daily imaging procedure, the total imaging dose equivalent per organ is plotted in
 285 figure 6. In general, the difference between $\text{CT}+28*\text{CBCT}$ and $\text{CT}+28*\text{X-ray}$ is low, as contribution from
 286 daily CBCT or X-ray is small when compared to the large contribution from CT.

287 4.3 Comparison between therapeutic and imaging dose equivalent per organ

288 For photon techniques the imaging dose equivalent is lower than the therapeutic dose equivalent. Still,
 289 close to the field, the contribution of imaging dose equivalent can be important (figure 6). For example,
 290 for the scapula the imaging dose equivalent for daily CBCT imaging is 29%, 24% and 24% of the dose
 291 equivalent during respectively 3D-CRT, IMRT and VMAT. When comparing imaging dose equivalent
 292 per organ to proton therapy, data become more comparable due to the lower out-of-field therapeutic dose
 293 equivalent during proton therapy. In organs close to the field the imaging dose equivalent even exceeds the
 294 therapeutic dose. For example, in scapula we observe that the imaging dose equivalent is 59% and 52%
 295 higher, respectively for daily CBCT and X-ray imaging, compared to proton therapeutic dose equivalent.
 296 The largest ratios between imaging dose equivalent and proton therapeutic dose are obtained in the sternum,
 297 with ratios of 3.6 and 3.2 for daily CBCT and X-ray imaging, respectively. In the abdomen region, the dose
 298 equivalent from imaging becomes smaller than the therapeutic dose during proton therapy as it can be seen
 299 for pancreas and other organs further away from the target.

300 4.4 Total dose equivalent per organ and comparison between radiotherapy techniques

301 A final comparison between radiotherapy techniques is made by considering the additional dose equivalent
 302 from imaging. Here we use the daily CBCT as the most conservative approach, as it resulted in the most
 303 elevated imaging dose equivalent, and compare the total dose equivalent for the different radiotherapy
 304 techniques in figure 7. Even when considering the contribution from imaging to the out-of-field dose
 305 equivalent during PBS proton therapy, the dose equivalent per organ is significantly lower when compared
 306 to photon radiotherapy. Within photon radiotherapy techniques, differences between techniques become

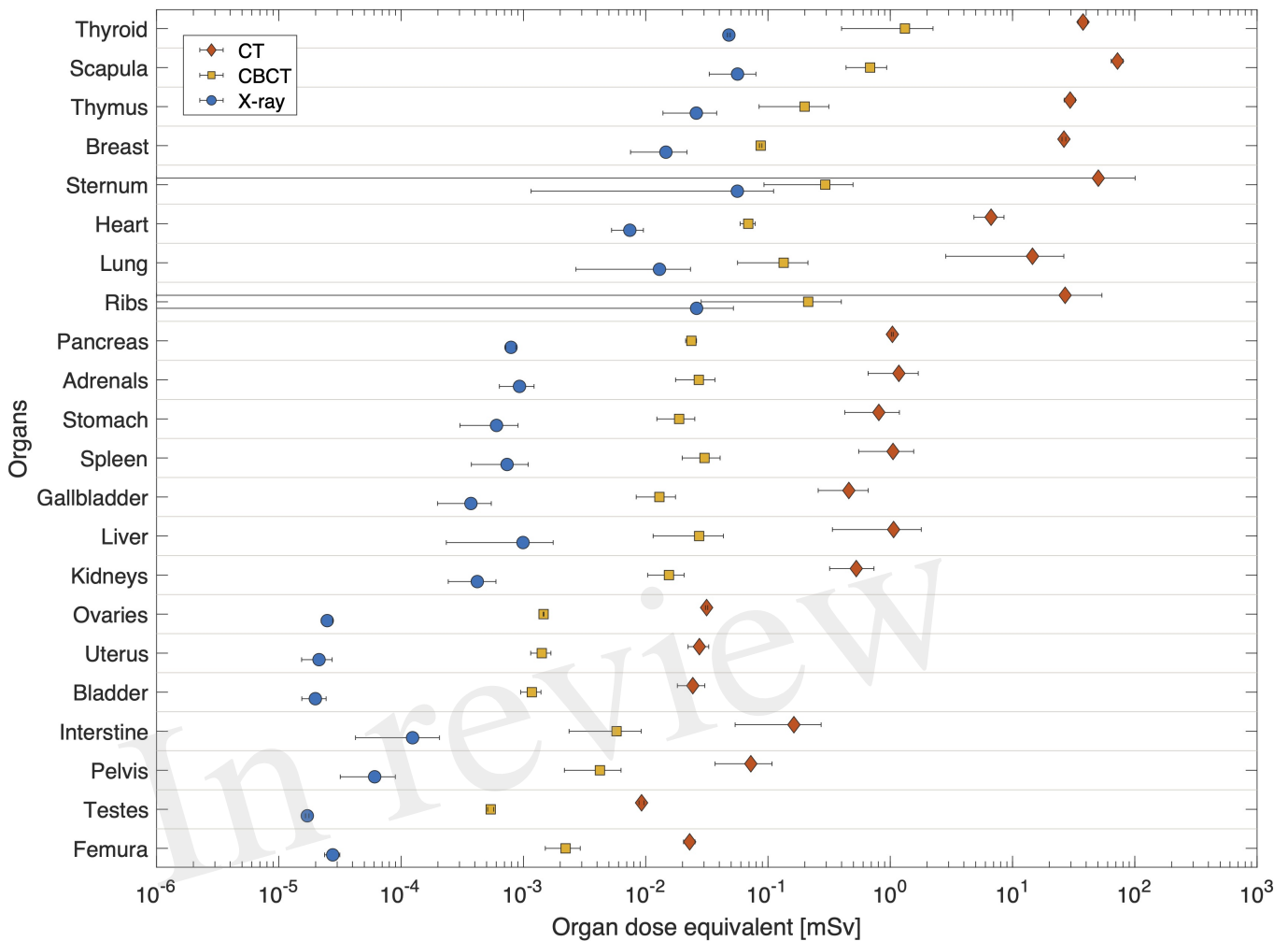


Figure 5. Average dose equivalent per organ for single imaging procedures using a: CT (left), kV-CBCT (middle) and X-ray (right). Organs are sorted according to their distance to target. Horizontal bars correspond the the spread of dose equivalent as calculated at various plugs inside the organ.

307 more visible the further away from the target. Clearly, IMRT yielded the most elevated out-of-field dose
 308 equivalent per organ.

309 The ratio of photon to proton dose equivalent increases when computed further away from the target. In
 310 the thyroid the ratio is around 4 for all photon techniques, while for the bladder the ratio is 36, 58 and 17
 311 when comparing 3D-CRT, IMRT and VMAT, respectively to PBS proton therapy.

312 4.5 LAR for secondary cancer

313 In table 1 LAR is shown for a limited number of organs for which dose-response relationships for cancer
 314 induction are available. We tabulated the LAR for each radiotherapy technique and imaging procedure
 315 individually as well as the summed LAR for the total doses. It is clear that the most pronounced risk is
 316 to develop breast cancer, followed by lung cancer and thyroid cancer. Proton therapy has a reduced risk
 317 compared to photon radiotherapy techniques, for the computed out-of-field dose distributions, which is

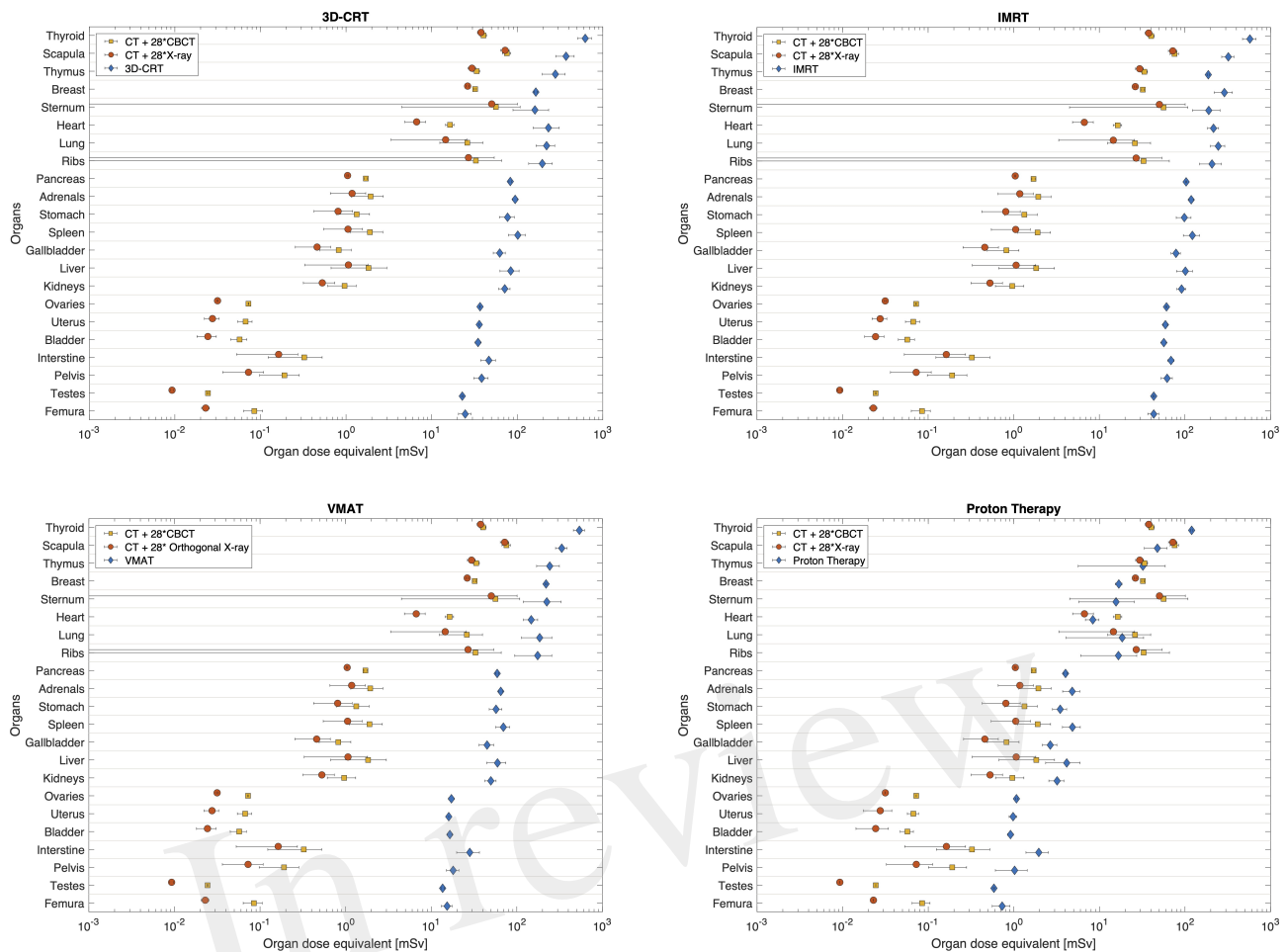


Figure 6. Comparison between total imaging dose equivalent for both, daily CBCT (CT+28*CBCT) and daily X-ray (CT+28*X-ray), as compared to 3D-CRT, IMRT, VMAT and proton PBS therapy. Organs are sorted according to their distance to target. Horizontal bars correspond the the spread of dose equivalent as computed at various plugs inside each organ.

318 respectively a factor of 9, 13 and 9 for 3D-CRT, IMRT and VMAT. The summed risk for the selected
 319 peripheral organs from proton therapy is slightly lower than the risks from imaging, assuming daily
 320 CBCT (CT+28*CBCT). This is mostly because the predicted LAR, for breast and lung cancer, is higher
 321 for imaging while other organs show a lower predicted LARs for imaging. When combining the risk
 322 calculations, from all investigated organs and including risks from radiotherapy and imaging, the predicted
 323 summed risk is the largest for IMRT (3.6%) followed by 3D-CRT (2.6%) and VMAT (2.5%). Proton therapy
 324 yields the smallest total LAR (0.6%) which is a factor of 5, 6 and 4 lower when compared to 3D-CRT,
 325 IMRT and VMAT, respectively. It must be stressed that these risk estimations are done for peripheral organs
 326 and take only into account the risk derived from the respective peripheral absorbed dose distributions
 327 obtained from treatment and therapeutic imaging. The summed risk for the considered peripheral organs
 328 will be hereafter referred to as ‘partial risk’.

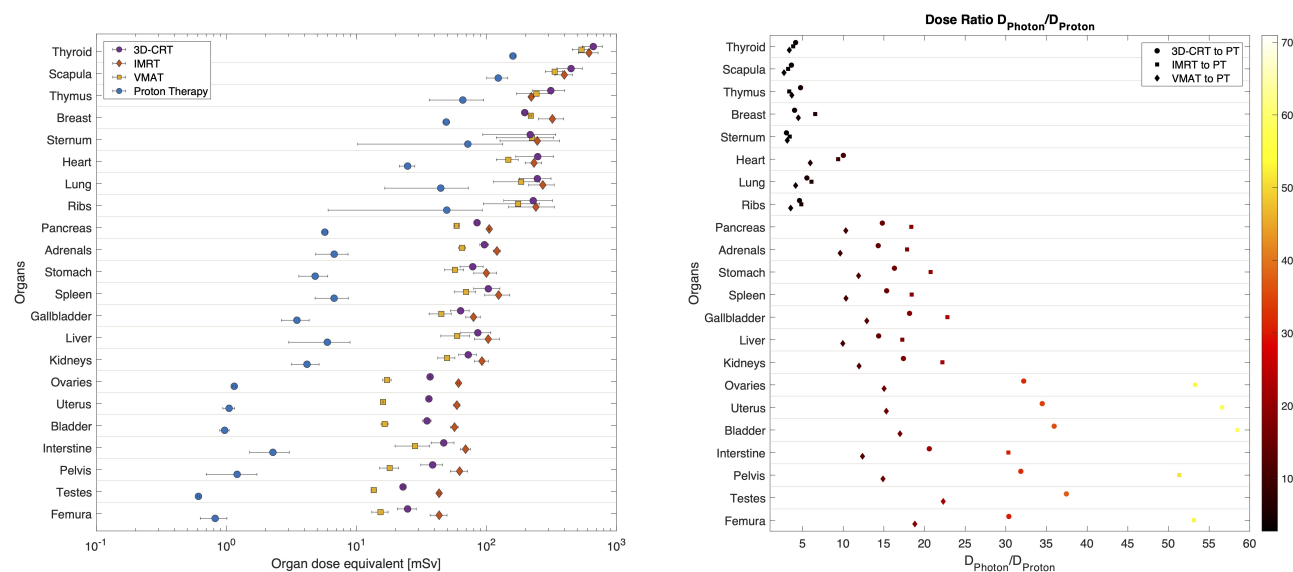


Figure 7. Total dose equivalent per organ calculated for 3D-CRT, IMRT, VMAT and PBS proton therapy, considering a daily CBCT imaging. On the right the photon (3D-CRT, IMRT and VMAT) to proton dose equivalent ratio per organ and corresponding colourbar scale. Organs are sorted according to their distance to target. Horizontal bars correspond to the combined spread of dose equivalent as estimated at various plugs inside each organ.

5 DISCUSSION

329 The current Monte Carlo-based framework allows to study the complete patient exposure during paediatric
 330 brain cancer and the potential subsequent risks for secondary cancer induction from available dose-response
 331 models. The accuracy of the presented simulations was experimentally shown in previous publications.

332 Stray radiation in proton therapy is dominated by neutrons, therefore we considered the higher RBE,
 333 by applying the Q-factor of neutrons in the Monte Carlo software and reported on dose equivalent per
 334 organ, as described in De Saint-Hubert et al. (2022b). For photon therapy as well as imaging doses we
 335 considered the radiation type and assumed a $RBE=Q\text{-factor}=1$. In this way a fair comparison between
 336 the techniques is allowed as radiation type is considered. These results demonstrate dose equivalent per
 337 organ were between a few, up to around hundred mSv for proton therapy, while photon techniques are
 338 ranging between few tens up to few hundreds of mSv. Furthermore, to allow the comparison between the
 339 radiotherapy techniques we featured the same cranial tumour location, size and shape. Still, the treatment
 340 plans were established according to the protocols of the individual radiotherapy clinics. These protocols
 341 differed regarding the requirements for PTV coverage (see section 3.1), which caused small dose deviations
 342 within the PTV. For instance, the median doses of the PTV exhibited differences of up to 2.7%. If these
 343 deviations are regarded as uncertainties, the impact on the overall uncertainties is negligible.

344 In the study from Knežević et al. (2022), the comparison between photon therapy, namely 3D-CRT, IMRT
 345 and GammaKnife, and PBS proton therapy for brain, revealed a reduction in out-of-field dose equivalent
 346 which was at the level of one order of magnitude close to the brain and more than two orders of magnitude
 347 further away from the target. Our study showed a similar benefit of proton therapy further away from the
 348 field, up to a factor of 58 for bladder when IMRT was compared to proton therapy. Nevertheless, we did
 349 not observe differences of more than two orders of magnitude, which could be due to several reasons. First,

LAR (%)					
	3D-CRT	IMRT	VMAT	Proton Therapy	Imaging
Bladder	0.08	0.12	0.04	0.002	0.000
Breast	1.18	2.04	1.34	0.124	0.236
Liver	0.10	0.11	0.07	0.005	0.002
Lungs	0.45	0.50	0.33	0.039	0.055
Stomach	0.14	0.18	0.10	0.006	0.002
Thyroid	0.37	0.34	0.30	0.076	0.026
Partial risk	2.32	3.30	2.17	0.25	0.32
3D-CRT + Imaging IMRT + Imaging VMAT + Imaging Proton Therapy + Imaging					
Bladder	0.08	0.12	0.04	0.002	
Breast	1.41	2.26	1.56	0.358	
Liver	0.10	0.12	0.07	0.007	
Lungs	0.50	0.55	0.38	0.094	
Stomach	0.14	0.18	0.11	0.009	
Thyroid	0.39	0.36	0.32	0.100	
Partial risk	2.62	3.60	2.48	0.57	

Table 1. LAR for selected peripheral organs and summed LAR for those organs (partial risk). LAR is computed for each radiotherapy technique and imaging procedure separately, as well as for the total doses of combined radiotherapy imaging procedures.

350 the present study reported on dose equivalent per organ resulting from a larger target volume (195.2 cm³)
351 compared to the previous study (65 cm³ (Knežević et al., 2022; Wochnik et al., 2021)). Another previous
352 study has shown the impact of clinical plan parameters on ambient neutron dose equivalent, H*(10), in
353 PBS proton therapy as a function of treatment plan parameters. The linear increase with field size and
354 an increase of up to a factor of 8 with an augmenting range were found to be the strongest influences
355 on H*(10) (Van Hoey and Parisi, 2021). Secondly, the present study used range shifters during PBS
356 proton treatment while this was not the case in the work of Knežević et al. (2022). Indeed, it has been
357 demonstrated that the use of a range shifter can increase the out-of-field dose up to more than a factor
358 of 2 (Wochnik et al., 2021; Van Hoey et al., 2022). Finally, the contribution of imaging procedures was
359 not considered in any previous study. Indeed, we noticed a more significant relative contribution, of the
360 dose equivalent per organ, from imaging when proton PBS therapy is applied when compared to photon
361 therapy. Another reason could be the fact that in the comparative study of Knežević et al., 3D-CRT was
362 done using dynamic and mechanical wedges increasing the out-of-field doses for this technique and hence
363 the ratio of photon to proton dose. Knežević et al. reported lowest out-of-field dose equivalent for IMRT
364 when compared to 3D-CRT and GammaKnife, which may be explained by the relatively low number of
365 monitoring units (209 MU) and the use of wedges during 3D-CRT. Herein, IMRT was performed with
366 682 MU and it should be noted that intensity modulation affects the out-of-field dose equivalent in two
367 ways. First, the collimator scatter is increased by a factor roughly proportional to the increase in monitor
368 units. Secondly, due to better conformality, patient scatter is decreased. The higher out-of-field dose for
369 IMRT when compared to 3D-CRT, suggests that the MU increase from 3D-CRT to IMRT is greater than

370 the reduction in patient scatter due to better conformality. Therefore, our work shows an increased risk of
371 secondary cancer induction for IMRT when compared to 3D-CRT. For VMAT (421 MU), on the other hand,
372 monitor units do not increase as much as with IMRT and, therefore, the advantage of better conformality
373 (less patient scatter) prevails and the risk for secondary cancer is below that of 3D-CRT.

374 One needs to be cautious when favoring one technique to another as this comparison is only for the
375 specific out-of-field organs considered for which measurements were performed. Indeed, the published
376 cancer risks represent only an under-estimation of the probable overall risk of secondary cancer, which
377 should include sarcoma, non-malignant brain tumors (e.g. meningioma), carcinoma for organs located
378 in-field and hematopoietic tumors for the overall risk ratio. It must also be pointed out that the cancer risks
379 for organs in the medium and high dose range can behave quite differently with regard to the various
380 irradiation techniques than in the low dose range (Sigurdson et al., 2005; Shuryak et al., 2009). This is
381 because the dose distribution of the primary radiation is more or less independent of the dose deposition by
382 scattered radiation (which is responsible for the peripheral dose deposition). Therefore, one cannot infer the
383 overall cancer risk from a comparison of the risks of different irradiation techniques for peripheral organs.
384 The cancer risk presentation should be understood as an example of quantitative risk assessment from dose
385 data. One goal of the HARMONIC project is to assess second cancer risk in relation to out-of-field organ
386 doses, with the aim of improving such risk models.

387 Imaging dose equivalent was most pronounced for CT and more than one order of magnitude higher when
388 compared to CBCT. CT dose equivalent data were, however, higher when compared to the data obtained
389 within the EPI-CT study (Thierry-Chef et al., 2021). For example, in EPI-CT the thyroid dose equivalent to
390 a 5-year-old CT scan of the brain was around 10 mSv, while in our study it was 38 mSv. The higher dose
391 equivalent observed in the presented CT exam may be due to several factors. First, the scan covered a larger
392 section of the patient's body compared to the EPI-CT study, where thyroid was out-of-field. Scan length
393 was shown to play a crucial role and effective dose was increased as a function of length with 15%/cm on
394 average (Wulff et al., 2021). Additionally, EPI-CT being a radiology study, protocols may be better adapted
395 to the patient morphology. In contrast, planning CT scanners typically use fewer protocols often relying on
396 a single kVp setting. This led, in our case, to the use of 120 kVp, even for head and paediatric exams where
397 lower voltage settings would have been preferred in diagnostic radiology. Moreover, the protocol used did
398 not apply current modulation techniques to reduce radiation exposure and spare dose in thin regions of the
399 patient's body, such as the neck region.

400 CBCT yielded dose equivalent data that were lower when compared to previously published data (Hälg
401 et al., 2014). Our study calculated doses between one mSv, close to the field and less than a μ Sv at far
402 distances while in the study from Hälg et al. (2014) kV-CBCT dose data from different manufacturers,
403 range between an average dose around 10 mGy at 10 cm and 0.1 mGy at 50 cm from the isocentre. Although
404 there may appear to be discrepancies, the reported doses are actually compatible. In fact, our 'head low
405 dose' protocol is similar to the 'high quality head' protocol (Hälg et al., 2012), with the main distinction
406 being that the high-quality protocol uses 5 times more mAs (due to different image quality target), which
407 directly translates to delivering 5 times more radiation dose to the patient. Moreover, reported organ doses
408 cannot be easily compared directly since the treatment site and the region in the two studies are different.

409 The dose equivalent from X-ray imaging was more than one order of magnitude lower than kV-CBCT.
410 We would like to note that during the first treatment session, the 'Kopf Kind G0A' protocol is repeated one
411 additional time at each one of the three gantry angles used by the proton treatment (70°, 110°, 260°). The
412 extra X-ray procedures are only done at the first radiotherapy treatment but we have calculated the impact
413 of this extra dose. As expected the dose equivalent from X-ray procedure increased and this was on average

414 by a factor of 3, when compared to a single angle (gantry 0°). However, this was only for the first treatment
415 fraction and the impact on the total dose equivalent was within 15%. Therefore, we did not report on the
416 extra dose from different angles. Moreover, X-ray doses are so low that the contribution to the total dose
417 equivalent will be very limited. For this reason, the total dose equivalent applied during radiotherapy was
418 calculated for daily OBI with kV-CBCT, which would result in the most conservative estimate of the dose
419 equivalent per organ and associated risk.

420 Typically, bone structures receive higher doses than soft tissues at similar distances from the field. This is
421 expected due to the energy range of photons used for imaging and the resulting higher mass attenuation
422 coefficient of bones compared to soft tissues. Additionally, dose spread appears to be greater in bones.
423 High dose gradients are particularly noticeable in organs such as the sternum, lungs, and ribs for CT and
424 X-ray. In these cases, the extreme dose spread could be attributed to the fact that, for both CT and X-ray,
425 the dose fall-off is located in the lung region, while for CBCT, it is in the neck area due to its smaller
426 imaging field of view measuring only 17 cm along the patient's length, compared to approximately 30 cm
427 for the other modalities. Overall, the importance of imaging dose is highlighted in our study (Bowles
428 et al., 2021) and strengthens the necessity to increase awareness on CT procedures (Smith-Bindman et al.,
429 2019; Bos et al., 2022) as well as on-board imaging in this specific application, namely radiotherapy in
430 paediatric populations (Korremans et al., 2010; Ding et al., 2018). The relative contribution from imaging
431 to the total dose equivalent per organ is more pronounced for proton therapy when compared to photon
432 therapy techniques. This is also reflected in the associated risks, demonstrating a similar risk from imaging
433 and therapeutic exposure. Risk of second cancers for far out-of-field organs may account for less than 20%
434 of all second cancers developed (even though this proportion depends on the follow-up time and attained
435 aged considered) (Diallo et al., 2009). The computed risk of secondary cancer following 3D-CRT, IMRT,
436 VMAT and PBS proton therapy are, respectively, 2.6%, 3.6%, 2.5% and 0.6%, which is in line with the
437 study from Xiang et al. (2020) that also suggests a lower risk for secondary cancer when using protons,
438 while IMRT and 3D-CRT showed similar risks. More specifically, for primary tumours of the head and
439 neck, proton therapy was associated with a significantly lower risk for secondary cancer (adjusted [OR],
440 0.42; 95% CI, 0.22–0.81; $P = 0.009$). In our study the risk was reduced by a factor of 6 when studying
441 protons versus IMRT, which could be related to the fact that we did not calculate the risk to all organs,
442 because of missing dose-response relationship for some organs, as well as the fact that we considered
443 only organs far out-of-field. Moreover, the study of Xiang et al. (2020) showed a modest decreased risk
444 of secondary cancer for head and neck cancer treated with IMRT when compared to 3D-CRT (adjusted
445 [OR], 0.85; 95% CI, 0.77–0.94; $P = 0.001$). This was not observed in the current study, where the risk
446 estimations show a reduced risk for 3D-CRT compared to IMRT. One possible explanation is that this work
447 only analyzes the cancer risk for organs in the low-dose volume. However, in the low dose volume, the
448 increased scatter and leakage dose with IMRT contributes to an increased cancer risk for these organs. For
449 organs that are in the high-dose range and not included in this study, IMRT reduces cancer risk because
450 of the higher conformality relative to 3D-CRT. Moreover, it should be noted that the study of Xiang et al.
451 (2020) was based on a short follow-up time when considering secondary cancer, especially those which
452 may arise in the low dose region.

453 The results of the present study should be considered under certain limitations. First, our results are
454 specific for the type of brain cancer studied and cannot be directly applied to other malignancies. Secondly,
455 the calculated doses are based on a CIRS phantom and, thus obtained for the given geometry and material
456 composition of this phantom. CIRS has developed materials that mimic the linear attenuation curves of
457 real tissue but the material composition is, of course, different from actual tissue. In the case of proton
458 therapy, in which the out-of-field dose is dominated by secondary neutrons, the material composition may

459 impact on the obtained doses. Thirdly, the organ dosimetry is done under certain assumptions such as
460 setting the RBE= Q -factor=1 for photon radiotherapy and all imaging procedures, as well as summing the
461 organ doses from the different procedures to get an overall dose equivalent per organ. The latter is open
462 for debate, but no other methods have been described so far. Furthermore, the average organ doses are
463 compared as calculated based on point measurements within the organ and do not allow to compare organ
464 dose distributions or dose-volume histograms (DVH). Even though a simple analytical model for a fast 3D
465 assessment of out-of-field doses has been proposed for photon radiotherapy (Sánchez-Nieto et al., 2022),
466 the DVHs would not alter our findings due to the small dose gradient in the out-of-field organs. Finally,
467 the most important limitation is likely to be the risk model employed, which is based on epidemiological
468 studies from A-bomb survivors and Hodgkin's lymphoma adult patients. It is known that the accuracy of
469 the predictions of this model is limited, however, to the best of our knowledge, this is one of the most
470 adequate models currently available. Dedicated epidemiological studies on paediatric cohorts with modern
471 radiotherapy techniques are required. The HARMONIC project is building a European registry of children
472 and adolescents treated with modern radiotherapy techniques, which contains DICOM files, in addition
473 to clinical, biological and follow-up data. This database will effectively open the possibility to future
474 epidemiological studies to, in turn, improve current risk models.

6 CONCLUSION

475 In this study we demonstrated the use of a validated Monte Carlo framework calculating the complete
476 dose equivalent per organ, including the therapeutic and imaging procedures. We reported on the complete
477 patient exposure during paediatric brain cancer treatment, showing a significant contribution from imaging
478 to the out-of-field dose equivalent per organ when proton therapy is used, due to the lower dose equivalent
479 from proton therapy compared to photon therapy techniques. For the specific out-of-field organs studied, it
480 was shown that proton therapy allows to decrease the out-of-field doses and associated risk for secondary
481 cancer.

CONFLICT OF INTEREST STATEMENT

482 The authors declare that the research was conducted in the absence of any commercial or financial
483 relationships that could be construed as a potential conflict of interest.

AUTHOR CONTRIBUTIONS

484 MD: dose and risk calculations, data analysis, writing. GB: imaging dose simulations, writing. US:
485 treatment-planning, risk calculations, data analysis, writing. CB: treatment planning, imaging protocols,
486 writing-review. NV: proton simulations, writing-reviewing. JE: Monte Carlo geometry coding. JW:
487 proton simulations. FS: photon simulations. FS: photon simulations and data analysis. NR: data analysis.
488 JD: methodology, writing-review. FV: data analysis. SR: data analysis. MR: photon simulations, data
489 processing. ACS: CT scanner geometry, NJ: epidemiological analysis, writing-review. BT: clinical analysis,
490 writing-review. ITC: project coordinator, writing-review. LB: Monte Carlo simulations, conceptualization,
491 supervision, writing, writing-review, editing. All authors contributed to the article and approved the
492 submitted version.

FUNDING

493 The presented research has been funded by the HARMONIC project. The HARMONIC project (Health
494 effects of cArDiac fluoRoscOpy and MOderN radIotherapy in paediatricS) has received funding from the
495 Euratom research and training programme 2014-2018 under grant agreement No 847707.

496 ITC acknowledges support from the Spanish Ministry of Science and Innovation and State Research
497 Agency through the ‘Centro de Excelencia Severo Ochoa 2019-2023’ Program (CEX2018-000806-S), and
498 support from the Generalitat de Catalunya through the CERCA Program.

ACKNOWLEDGMENTS

499 The authors are thankful to Niklas Wahl from the matRad project.

REFERENCES

- 500 Agostinelli, S., Allison, J., Amako, K., Apostolakis, J., Araujo, H., Arce, P., et al. (2003). Geant4—A
501 simulation toolkit. *Nucl Instrum Meth A* 506, 250–303
- 502 Allison, J., Amako, K., Apostolakis, J., Araujo, H., Arce Dubois, P., Asai, M., et al. (2006). Geant4
503 developments and applications. *IEEE T Nucl Sci* 53, 270–278
- 504 Allison, J., Amako, K., Apostolakis, J., Arce, P., Asai, M., Aso, T., et al. (2016). Recent developments in
505 Geant4. *Nucl Instrum Meth A* 835, 186–225
- 506 Athar, B. S., Bednarz, B., Seco, J., Hancox, C., and Paganetti, H. (2010). Comparison of out-of-field
507 photon doses in 6 MV IMRT and neutron doses in proton therapy for adult and pediatric patients. *Phys*
508 *Med Biol* 55, 2879–2891
- 509 Baró, J., Sempau, J., Fernández-Varea, J., and Salvat, F. (1995). PENELOPE: An algorithm for Monte
510 Carlo simulation of the penetration and energy loss of electrons and positrons in matter. *Nucl Inst Meth*
511 *B* 100, 31–46
- 512 Boissonnat, G., Chesneau, H., Barat, E., Dautremer, T., Garcia-Hernandez, J.-C., and Lazaro, D. (2020).
513 Validation of histogram-based virtual source models for different IGRT kV-imaging systems. *Med Phys*
514 47, 4531–4542
- 515 Bos, D., Yu, S., Luong, J., Chu, P., Wang, Y., Einstein, A., et al. (2022). Diagnostic reference levels and
516 median doses for common clinical indications of CT: findings from an international registry. *Eur Radiol*
517 32, 1971–1982
- 518 Bowles, E., Miglioretti, D., Kwan, M., Bartels, U., Furst, A., Cheng, S., et al. (2021). Long-term medical
519 imaging use in children with central nervous system tumors. *PLoS One* 21, e0248643
- 520 Chung, C. S., Yock, T. I., Nelson, K., Xu, Y., Keating, N. L., and Tarbell, N. J. (2013). Incidence of second
521 malignancies among patients treated with proton versus photon radiation. *Int J Radiat Oncol Biol Phys*
522 87, 46–52
- 523 [Dataset] CIRS (2013). ATOM dosimetry phantoms. [https://www.cirsinc.com/wp-content/
524 uploads/2021/06/701-706-ATOM-PB-062521.pdf](https://www.cirsinc.com/wp-content/uploads/2021/06/701-706-ATOM-PB-062521.pdf). Accessed: 2023-07-17
- 525 Constine, L., Ronckers, C., Hua, C.-H., Olch, A., Kremer, L., Jackson, A., et al. (2019). Pediatric normal
526 tissue effects in the clinic (PENTEC): An international collaboration to analyse normal tissue radiation
527 dose–volume response relationships for paediatric cancer patients. *Clin Oncol* 31, 199–207
- 528 De Saint-Hubert, M., Majer, M., Hršak, H., Heinrich, Z., Knežević, Z., Miljanic, S., et al. (2018). Out-of-
529 field doses in children treated for large arteriovenous malformations using hypofractionated Gamma
530 Knife radiosurgery and intensity-modulated radiation therapy. *Radiat Prot Dosim* 181, 100–110

- 531 De Saint-Hubert, M., Suesselbeck, F., Vasi, F., Stuckmann, F., Rodriguez, M., Dabin, J., et al. (2022a).
532 Experimental validation of an analytical program and a monte carlo simulation for the computation of
533 the far out-of-field dose in external beam photon therapy applied to pediatric patients. *Front Oncol* 12,
534 882506
- 535 De Saint-Hubert, M., Verbeek, N., Bäumer, C., Esser, J., Wulff, J., Nabha, R., et al. (2022b). Validation of
536 a Monte Carlo framework for out-of-field dose calculations in proton therapy. *Front Oncol* 12, 882489
- 537 De Saint-Hubert, M., Verellen, D., Poels, K., Crijns, W., Magliona, F., Depuydt, T., et al. (2017). Out-
538 of-field doses from pediatric craniospinal irradiations using 3D-CRT, IMRT, helical tomotherapy and
539 electron-based therapy. *Phys Med Biol* 62, 5293–5311
- 540 Diallo, I., Haddy, N., Adjadj, E., Samand, A., Quiniou, E., Chavaudra, J., et al. (2009). Frequency
541 distribution of second solid cancer locations in relation to the irradiated volume among 115 patients
542 treated for childhood cancer. *Int J Radiat Oncol Biol Phys* 74, 876–883
- 543 Ding, G. X., Alaei, P., Curran, B., Flynn, R., Gossman, M., Mackie, T. R., et al. (2018). Image guidance
544 doses delivered during radiotherapy: Quantification, management, and reduction: Report of the AAPM
545 Therapy Physics Committee Task Group 180. *Med Phys* 45, e84–e99
- 546 Domingo, C., Lagares, J. I., Romero-Expósito, M., Sánchez-Nieto, B., Nieto-Camero, J. J., Terrón, J. A.,
547 et al. (2022). Peripheral organ equivalent dose estimation procedure in proton therapy. *Front Oncol* 12,
548 882476
- 549 Geng, C., Moteabbed, M., Seco, J., Gao, Y., George Xu, X., Ramos-Méndez, J., et al. (2015). Dose
550 assessment for the fetus considering scattered and secondary radiation from photon and proton therapy
551 when treating a brain tumor of the mother. *Phys Med Biol* 61, 683–695
- 552 Gudowska, I., Ardenfors, O., Toma-Dasu, I., and Dasu, A. (2014). Radiation burden from secondary doses
553 to patients undergoing radiation therapy with photons and light ions and radiation doses from imaging
554 modalities. *Radiat Prot Dosim* 161, 357–62
- 555 Hälgl, R. A., Besserer, J., Boschung, M., Mayer, S., Lomax, A. J., and Schneider, U. (2014). Measurements
556 of the neutron dose equivalent for various radiation qualities, treatment machines and delivery techniques
557 in radiation therapy. *Phys Med Biol* 59, 2457–2468
- 558 Hälgl, R. A., Besserer, J., and Schneider, U. (2012). Systematic measurements of whole-body imaging dose
559 distributions in image-guided radiation therapy. *Med Phys* 39, 7650–7661
- 560 Harbron, R. W., Thierry-Chef, I., Pearce, M. S., Bernier, M.-O., Dreuil, S., Rage, E., et al. (2020). The
561 HARMONIC project: study design for the assessment of radiation doses and associated cancer risks
562 following cardiac fluoroscopy in childhood. *J Radiol Prot* 40, 1074
- 563 [Dataset] HARMONIC (2019). European Commission Horizon 2020 HARMONIC project website.
564 <https://harmonicproject.eu/>. Accessed: 2023-01-26
- 565 Hauptmann, M., Byrnes, G., Cardis, E., Bernier, M.-O., Blettner, M., Dabin, J., et al. (2023). Brain cancer
566 after radiation exposure from CT examinations of children and young adults: results from the EPI-CT
567 cohort study. *Lancet Oncol* 24, 45–53
- 568 Huang, W. Y., Muo, C. H., Lin, C. Y., Jen, Y. M., Yang, M. H., Lin, J. C., et al. (2014). Paediatric head
569 CT scan and subsequent risk of malignancy and benign brain tumour: a nation-wide population-based
570 cohort study. *Br J Cancer* 110, 2354–2360
- 571 Journy, N., Mansouri, I., Allodji, R. S., Demoor-Goldschmidt, C., Ghazi, D., Haddy, N., et al. (2019).
572 Volume effects of radiotherapy on the risk of second primary cancers: A systematic review of clinical
573 and epidemiological studies. *Radiother Oncol* 131, 150–159
- 574 Kalbasi, A., Kirk, M., Teo, B. K., Diffenderfer, E., Ding, X., McDonough, J., et al. (2018). Proton
575 craniospinal irradiation during the third trimester of pregnancy. *Pract Radiat Oncol* 8, 213–216

- 576 Kellerer, A. M., Nekolla, E. A., and Walsh, L. (2001). On the conversion of solid cancer excess relative
577 risk into lifetime attributable risk. *Radiat Environ Biophys* 40, 249–257
- 578 Knežević, Z., Ambrožová, I., Domingo, C., De Saint-Hubert, M., Majer, M., Martínez-Rovira, I., et al.
579 (2018). Comparison of response of passive dosimetry systems in scanning proton radiotherapy—a study
580 using paediatric anthropomorphic phantoms. *Radiat Prot Dosim* 180, 256–260
- 581 Knežević, Z., Stolarczyk, L., Ambrožová, I., Caballero-Pacheco, M. A., Davidková, M., De Saint-
582 Hubert, M., et al. (2022). Out-of-field doses produced by a proton scanning beam inside pediatric
583 anthropomorphic phantoms and their comparison with different photon modalities. *Front Oncol* 12,
584 904563
- 585 Korreman, S., Rasch, C., McNair, H., Verellen, D., Oelfke, U., Maingon, P., et al. (2010). The European
586 Society of Therapeutic Radiology and Oncology–European Institute of Radiotherapy (ESTRO–EIR)
587 report on 3D CT-based in-room image guidance systems: A practical and technical review and guide.
588 *Radiother Oncol* 94, 129–144
- 589 Le Deroff, C., Berger, L., Bellec, J., Boissonnat, G., Chesneau, H., Chiavassa, S., et al. (2022). Monte
590 Carlo-based software for 3D personalized dose calculations in image-guided radiotherapy. *Phys and
591 Imag Radiat Oncol* 21, 108–114
- 592 Majer, M., Ambrožová, I., Davidková, M., De Saint-Hubert, M., Kasabašić, M., Knežević, Z., et al. (2022).
593 Out-of-field doses in pediatric craniospinal irradiations with 3D-CRT, VMAT, and scanning proton
594 radiotherapy: A phantom study. *Med Phys* 49, 2672–2683
- 595 Majer, M., Stolarczyk, L., De Saint-Hubert, M., Kabat, D., Knežević, Z., Miljanic, S., et al. (2017).
596 Out-of-field dose measurements for 3D conformal and intensity modulated radiotherapy of a paediatric
597 brain tumour. *Radiat Prot Dosim* 176, 331–340
- 598 Mathews, J. D., Forsythe, A. V., Brady, Z., Butler, M. W., Goergen, S. K., Byrnes, G. B., et al. (2013).
599 Cancer risk in 680 000 people exposed to computed tomography scans in childhood or adolescence: data
600 linkage study of 11 million Australians. *BMJ* 346, f2360
- 601 Palmer, J., Tsang, D., Tinkle, C., Olch, A., Kremer, L., Ronckers, C., et al. (2021). Late effects of radiation
602 therapy in pediatric patients and survivorship. *Pediatr Blood Cancer* 68, e28349
- 603 Pearce, M. S., Salotti, J. A., Little, M. P., McHugh, K., Lee, C., Kim, K. P., et al. (2012). Radiation exposure
604 from CT scans in childhood and subsequent risk of leukaemia and brain tumours: a retrospective cohort
605 study. *Lancet* 380, 499–505
- 606 Perl, J., Shin, J., Schümann, J., Faddegon, B., and Paganetti, H. (2012). TOPAS: An innovative proton
607 Monte Carlo platform for research and clinical applications. *Med Phys* 39, 6818–6837
- 608 Pokora, R., Krille, L., Dreger, S., Lee, C., Günster, C., Zeeb, H., et al. (2016). Computed tomography in
609 Germany. *Dtsch Arztebl Int* 113, 721–728
- 610 Rodriguez, M. and Brualla, L. (2018). Many-integrated core (MIC) technology for accelerating Monte
611 Carlo simulation of radiation transport: A study based on the code DPM. *Comput Phys Commun* 225,
612 28–35
- 613 Rodriguez, M., Sempau, J., Bäumer, C., Timmermann, B., and Brualla, L. (2018). DPM as a radiation
614 transport engine for PRIMO. *Radiat Oncol* 13, 256
- 615 Rodriguez, M., Sempau, J., and Brualla, L. (2012). A combined approach of variance-reduction techniques
616 for the efficient Monte Carlo simulation of linacs. *Phys Med Biol* 57, 3013–3024
- 617 Rodriguez, M., Sempau, J., and Brualla, L. (2013). PRIMO: A graphical environment for the Monte Carlo
618 simulation of Varian and Elekta linacs. *Strahlenther Onkol* 189, 881–886
- 619 Rodriguez, M., Sempau, J., Fogliata, A., Cozzi, L., Sauerwein, W., and Brualla, L. (2015). A geometrical
620 model for the Monte Carlo simulation of the TrueBeam linac. *Phys Med Biol* 60, N219–N229

- 621 Schneider, U., Hälgl, R., and Besserer, J. (2015). Concept for quantifying the dose from image guided
622 radiotherapy. *Radiat Oncol* 17, 188
- 623 Schneider, U., Sumila, M., and Robotka, J. (2011). Site-specific dose-response relationships for cancer
624 induction from the combined Japanese A-bomb and Hodgkin cohorts for doses relevant to radiotherapy.
625 *Theor Biol Med Model* 8, 27
- 626 Sempau, J., Acosta, E., Baro, J., Fernández-Varea, J., and Salvat, F. (1997). An algorithm for Monte Carlo
627 simulation of coupled electron-photon transport. *Nucl Inst Meth B* 132, 377–390
- 628 Sempau, J., Badal, A., and Brualla, L. (2011). A PENELOPE based system for the automated Monte
629 Carlo simulation of clinacs and voxelized geometries, application to far from axis fields. *Med Phys* 38,
630 5887–5895
- 631 Sempau, J., Wilderman, S. J., and Bielajew, A. F. (2000). DPM, a fast, accurate Monte Carlo code
632 optimized for photon and electron radiotherapy treatment planning dose calculations. *Phys Med Biol* 45,
633 2263–2291
- 634 Shuryak, I., Hahnfeldt, P., Hlatky, L., Sachs, R., and Brenner, D. (2009). A new view of radiation-induced
635 cancer: integrating short- and long-term processes. Part II: second cancer risk estimation. *Radiat Environ*
636 *Biophys* 48, 275–286
- 637 Sigurdson, A., Ronckers, C., Mertens, A., Stovall, M., Smith, S., Liu, Y., et al. (2005). Primary thyroid
638 cancer after a first tumour in childhood (the Childhood Cancer SurvivorStudy): a nested case-control
639 study. *Lancet* 365, 2014–2023
- 640 Smith-Bindman, R., Wang, Y., Chu, P., Chung, R., Einstein, A., Balcombe, J., et al. (2019). International
641 variation in radiation dose for computed tomography examinations: prospective cohort study. *BMJ* 364,
642 k4931
- 643 Sánchez-Nieto, B., López-Martínez, I. N., Rodríguez-Mongua, J. L., and Espinoza, I. (2022). A simple
644 analytical model for a fast 3D assessment of peripheral photon dose during coplanar isocentric photon
645 radiotherapy. *Front Oncol* 12, 872752
- 646 Sánchez-Nieto, B., Romero-Expósito, M., Terrón, J. A., Irazola, L., Paiusco, M., Cagni, E., et al.
647 (2018). Intensity-modulated radiation therapy and volumetric modulated arc therapy versus conventional
648 conformal techniques at high energy: Dose assessment and impact on second primary cancer in the
649 out-of-field region. *Rep Pract Oncol Radiother* 23, 251–259
- 650 Thierry-Chef, I., Ferro, G., Le Cornet, L., Dabin, J., Istad, T. S., Jahnen, A., et al. (2021). Dose Estimation
651 for the European Epidemiological Study on Pediatric Computed Tomography (EPI-CT). *Radiat Res* 196,
652 74–99
- 653 Van Hoey, O. and Parisi, A. (2021). Development and validation of a model for assessing neutron fluence
654 with lithium fluoride thermoluminescent detectors. *Radiat Phys Chem* 188, 109688
- 655 Van Hoey, O., Stolarczyk, L., Lillhök, J., Eliasson, L., Mojzeszek, N., Liszka, M., et al. (2022). Simulation
656 and experimental verification of ambient neutron doses in a pencil beam scanning proton therapy room
657 as a function of treatment plan parameters. *Front Oncol* 12, 903537
- 658 Wang, Y., Kremer, L., Leeuwen, F., Armstrong, G., Leisenring, W., de Vathaire, F., et al. (2022). Cohort
659 profile: Risk and risk factors for female breast cancer after treatment for childhood and adolescent cancer:
660 an internationally pooled cohort. *BMJ open* 12, e065910
- 661 Weber, D. C., Habrand, J. L., Hoppe, B. S., Hill Kayser, C., Laack, N. N., Langendijk, J. A., et al. (2018).
662 Proton therapy for pediatric malignancies: Fact, figures and costs. A joint consensus statement from the
663 pediatric subcommittee of PTCOG, PROS and EPTN. *Radiother Oncol* 128, 44–55
- 664 Wieser, H., Cisternas, E., Wahl, N., Ulrich, S., Stadler, A., Mescher, H., et al. (2017). Development of the
665 open-source dose calculation and optimization toolkit matRad. *Med Phys* 44, 2556–2568

- 666 Wochnik, A., Stolarczyk, L., Ambrožová, I., Davídková, M., De Saint-Hubert, M., Domański, S., et al.
667 (2021). Out-of-field doses for scanning proton radiotherapy of shallowly located paediatric tumours—a
668 comparison of range shifter and 3D printed compensator. *Phys Med Biol* 66, 035012
- 669 Wulff, J., Schmidt, R., Bäumer, C., Timmermann, B., and Zink, K. (2021). PO-1786 Computed tomography
670 of the head for therapy planning of pediatric patients—impact of scan-length. *Radiother Oncol* 161,
671 S1512
- 672 Xiang, M., Chang, D. T., and Pollom, E. L. (2020). Second cancer risk after primary cancer treatment
673 with three-dimensional conformal, intensity-modulated, or proton beam radiation therapy. *Cancer* 126,
674 3560–3568
- 675 Yeom, Y. S., Griffin, K. T., Mille, M. M., Lee, C., O'Reilly, S., Dong, L., et al. (2022). Fetal dose from
676 proton pencil beam scanning craniospinal irradiation during pregnancy: a Monte Carlo study. *Phys Med*
677 *Biol* 67
- 678 Yeom, Y. S., Kuzmin, G., Griffin, K., Mille, M., Polf, J., Langner, U., et al. (2020). A Monte Carlo model
679 for organ dose reconstruction of patients in pencil beam scanning (PBS) proton therapy for epidemiologic
680 studies of late effects. *J Radiol Prot* 40, 225–242

In review

Figure 1.JPEG

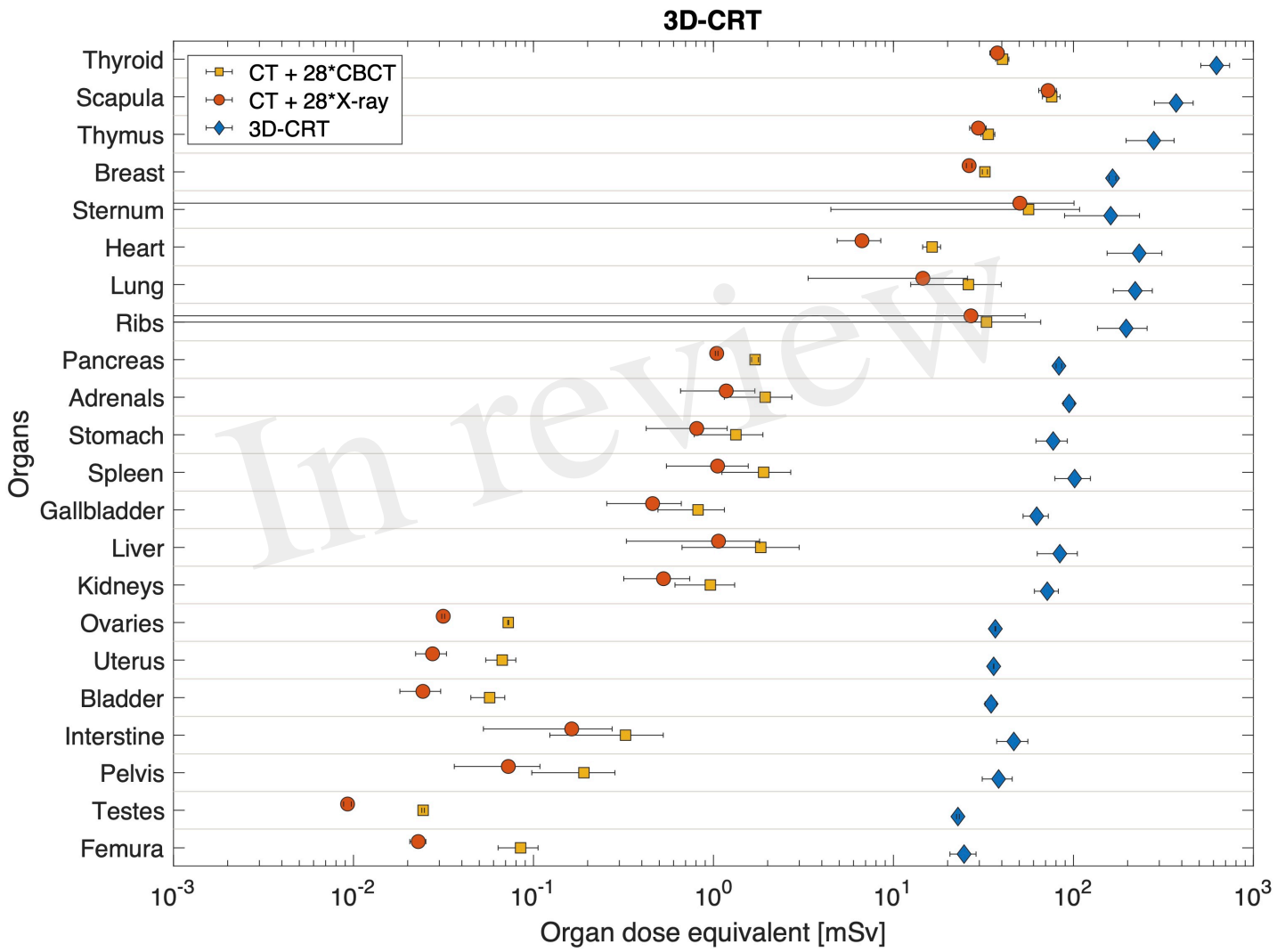


Figure 2.JPEG

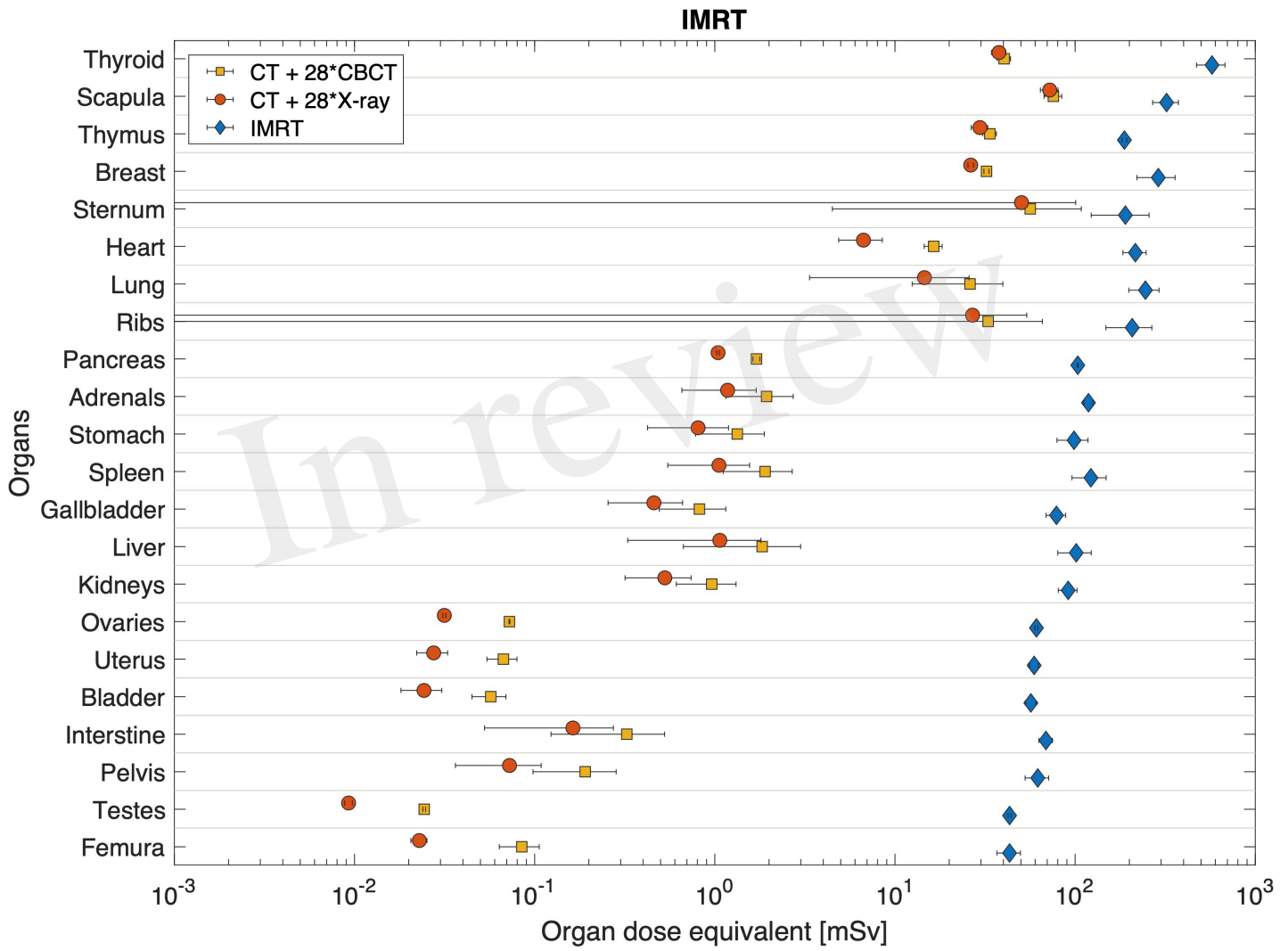


Figure 3.JPEG

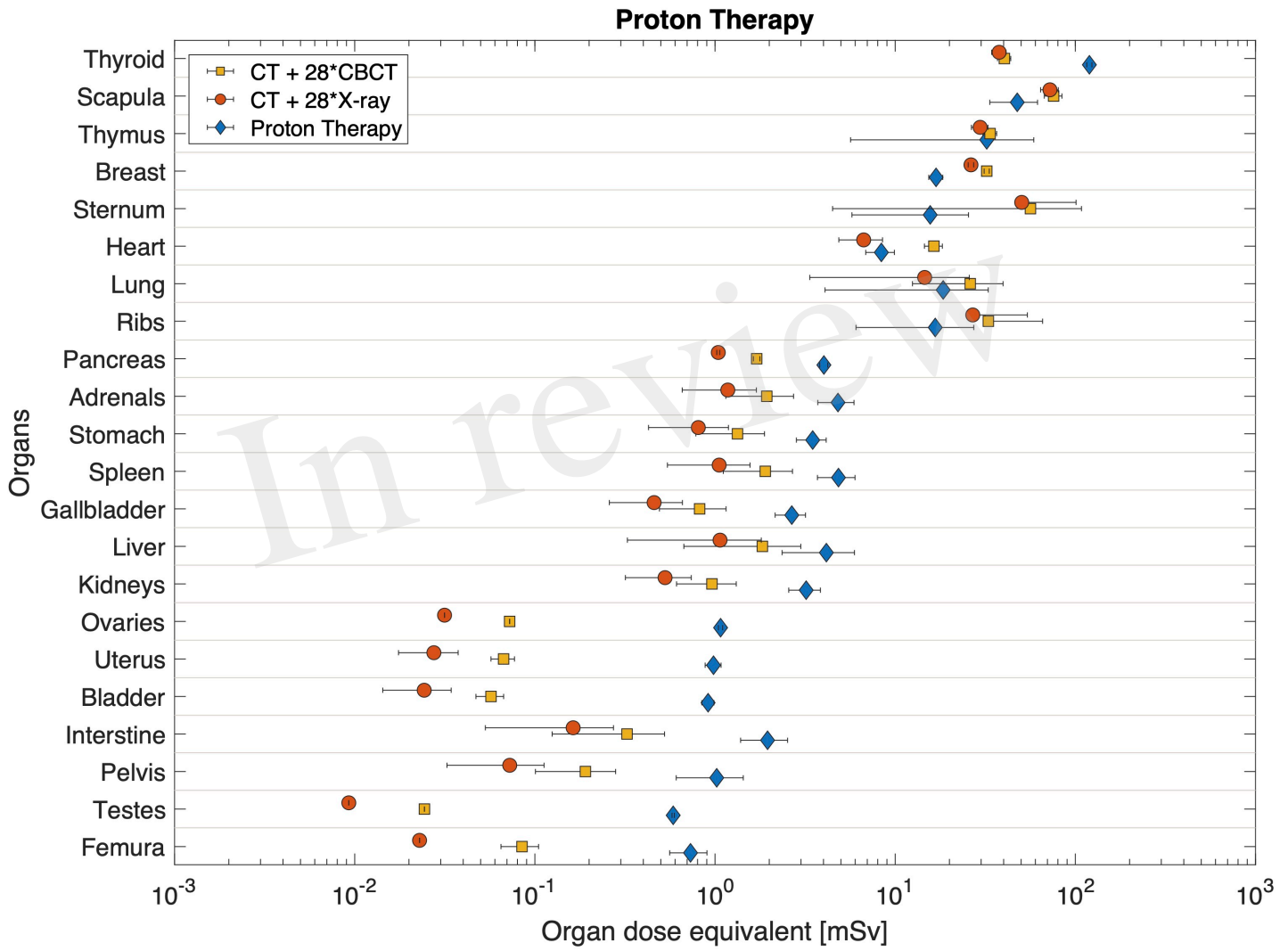


Figure 4.JPEG

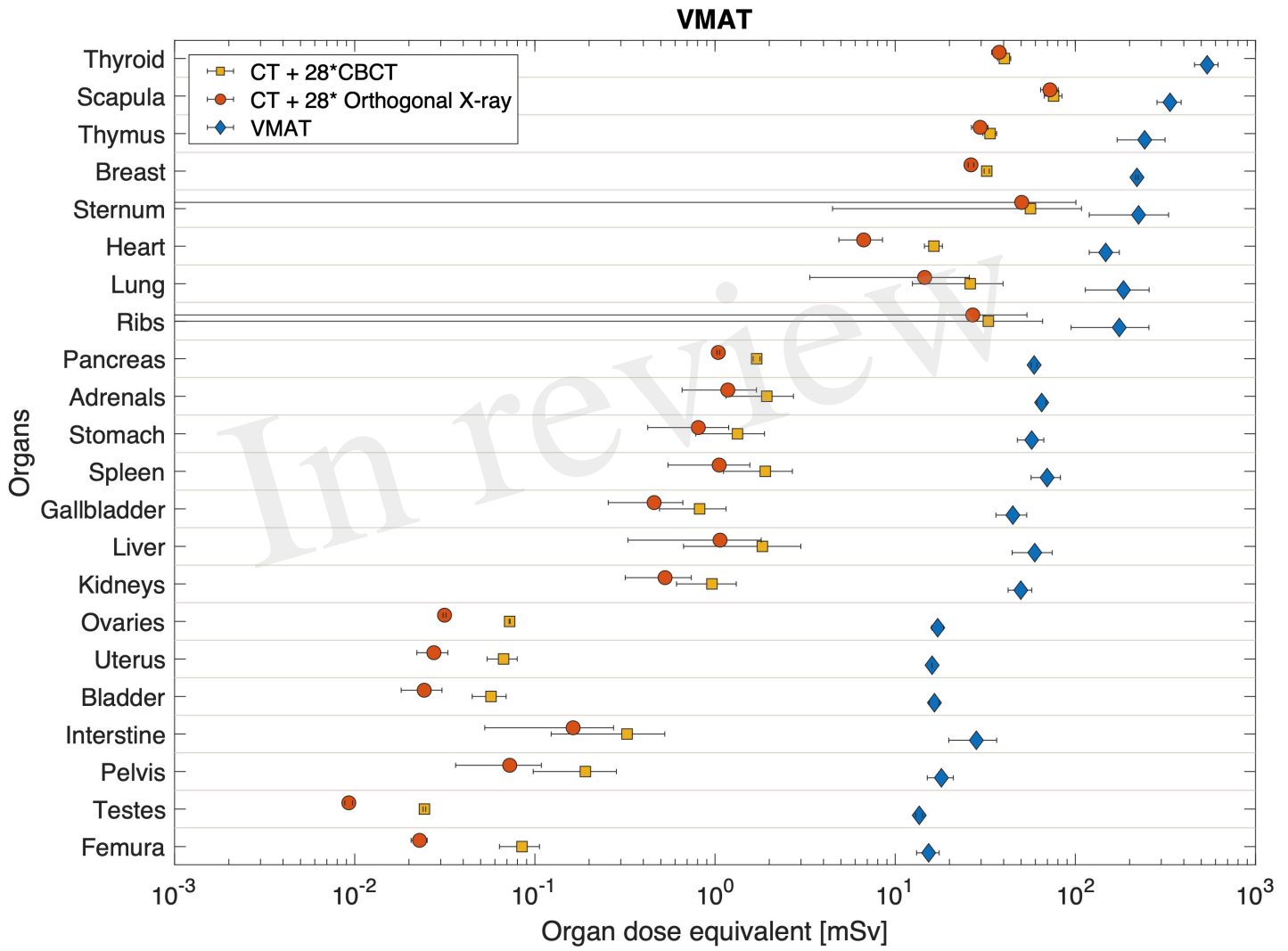


Figure 5.JPEG

BigBore - 120kV - 12 mm collimation
pitch = 0.813 - table speed = 13 mm/s (mean current = 90.92 mA)

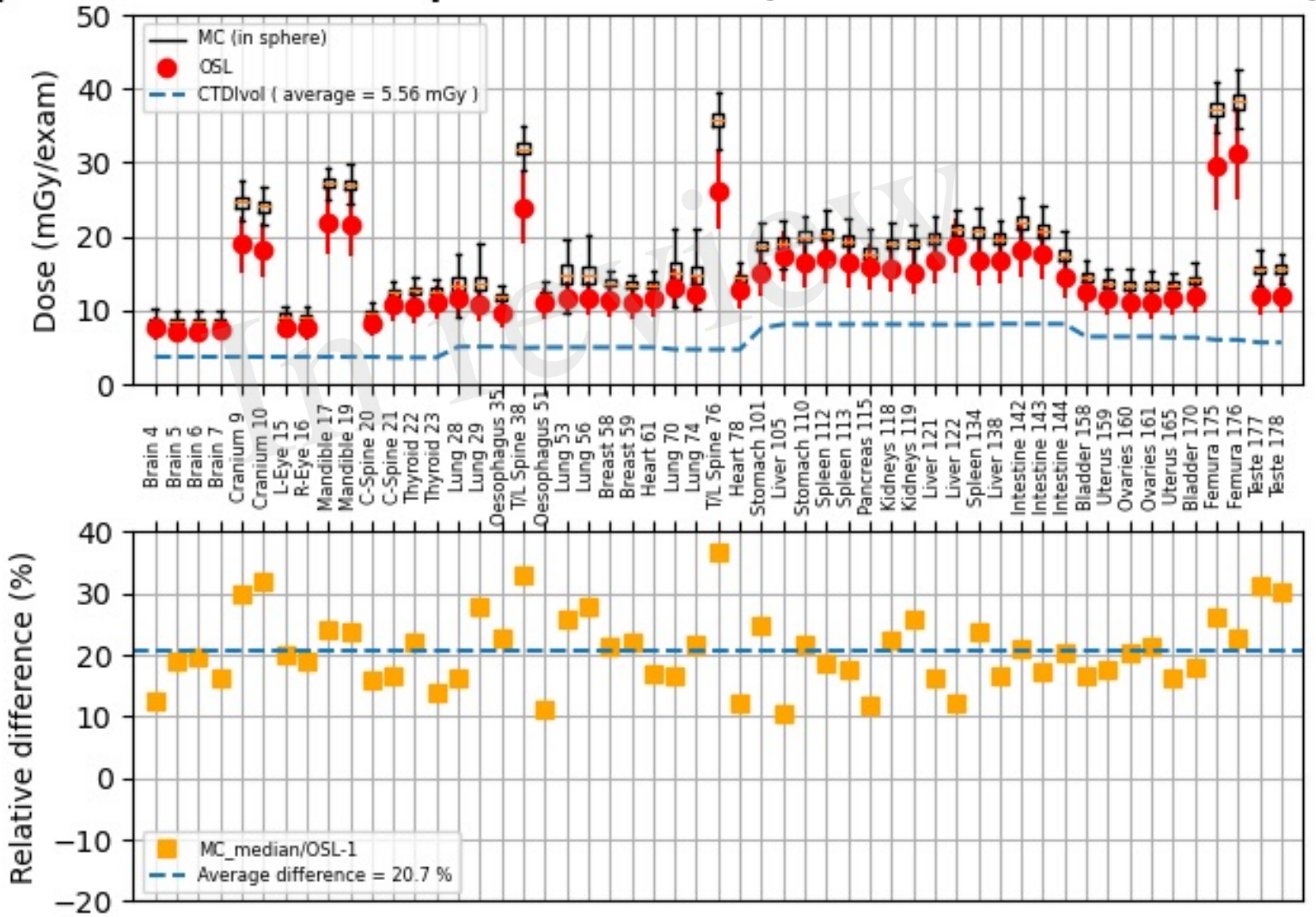


Figure 6.JPEG

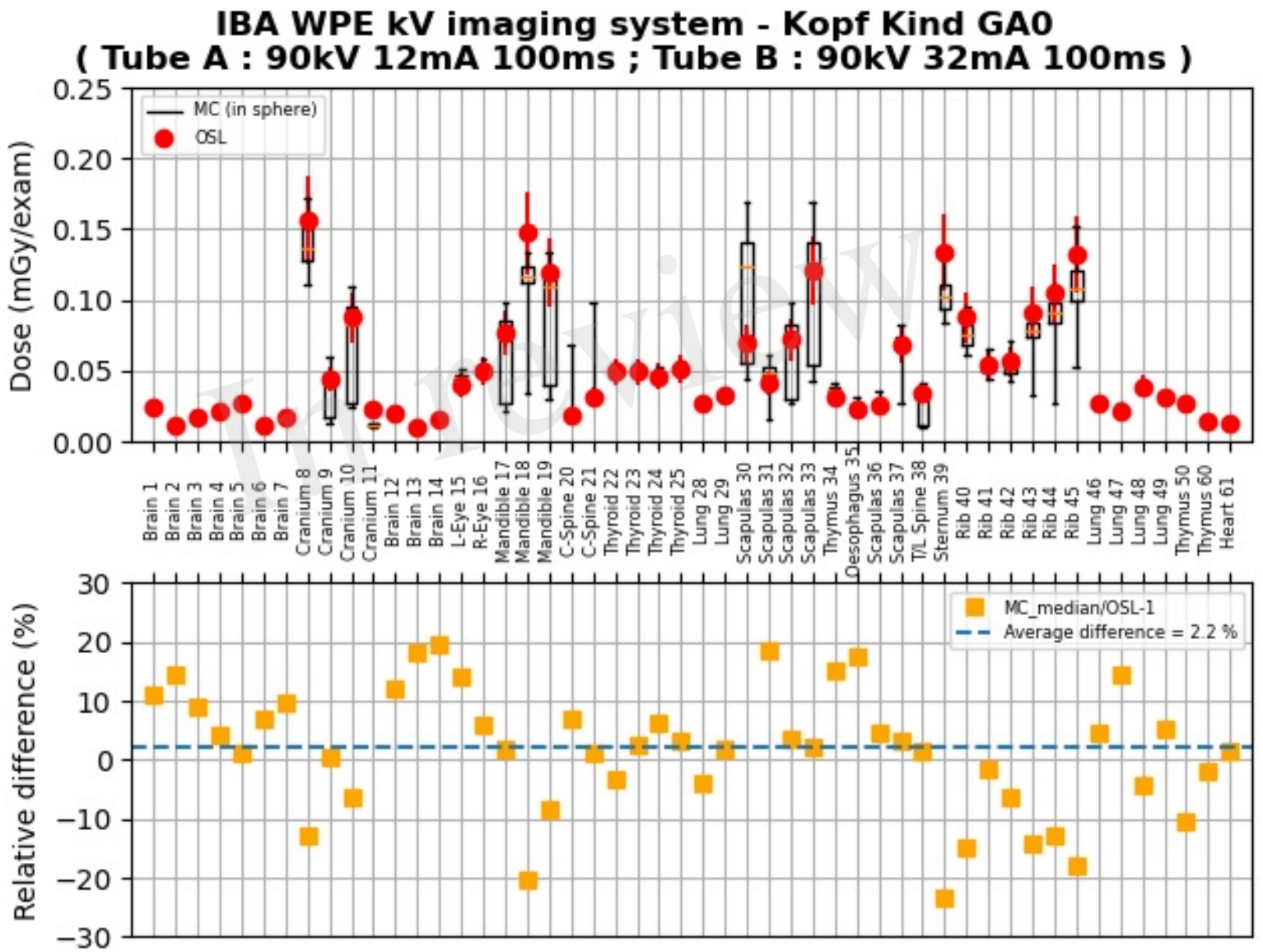


Figure 7.JPEG

In review

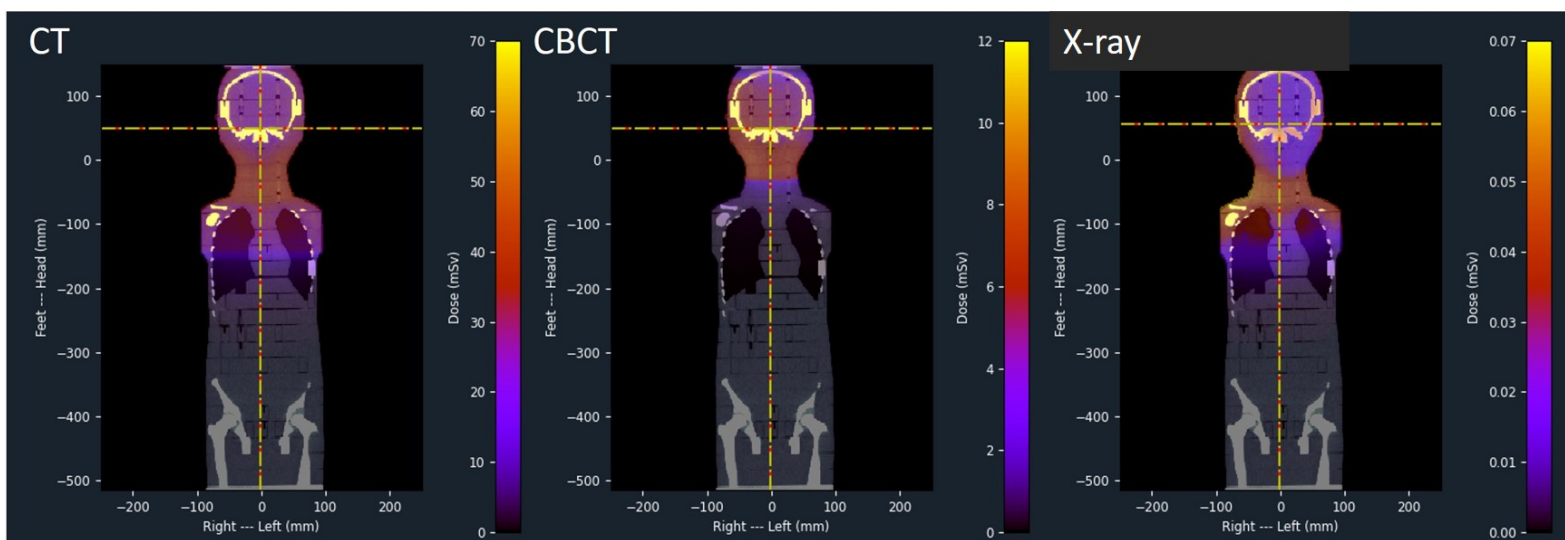


Figure 8.JPEG

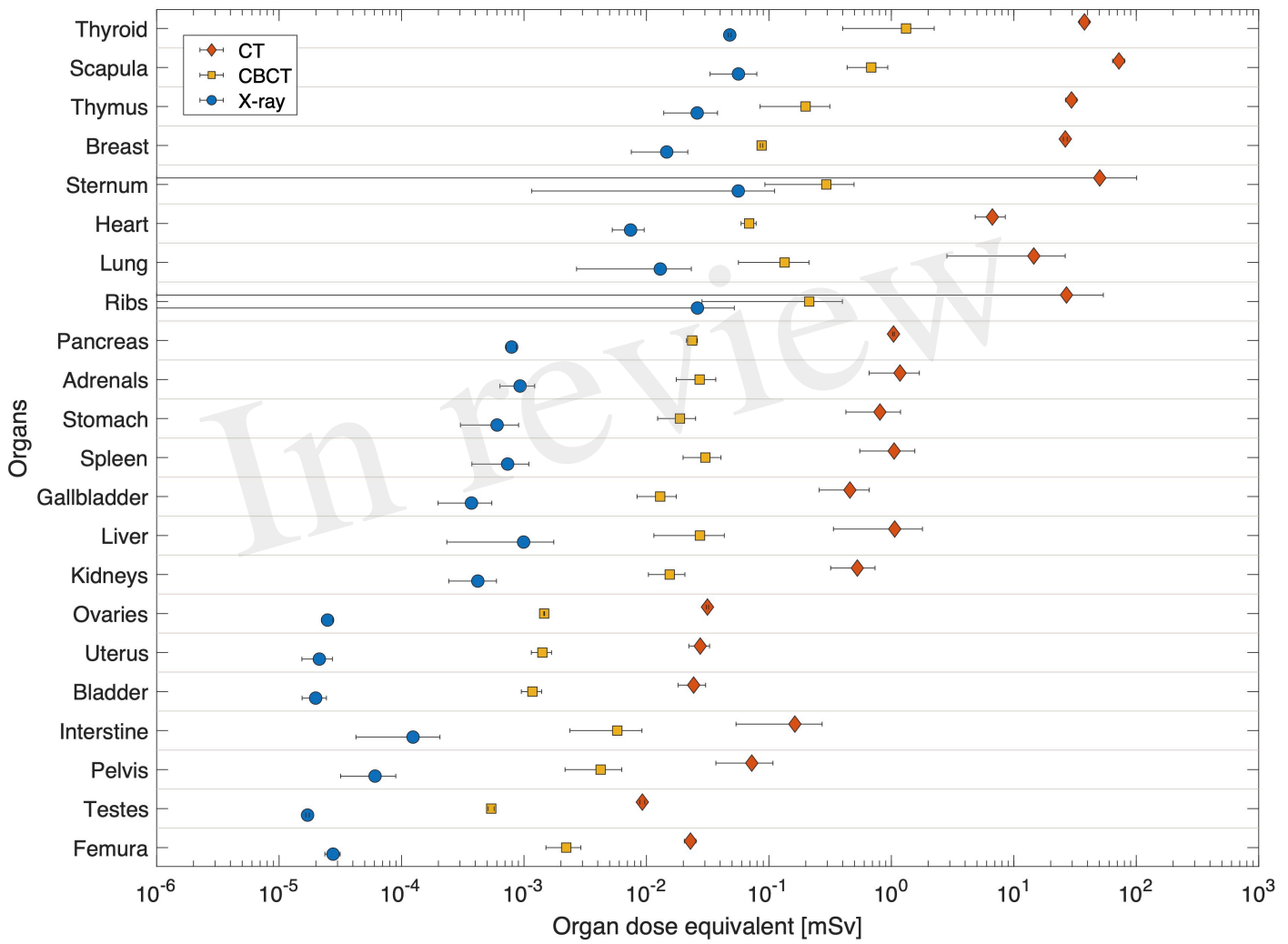


Figure 9.JPEG

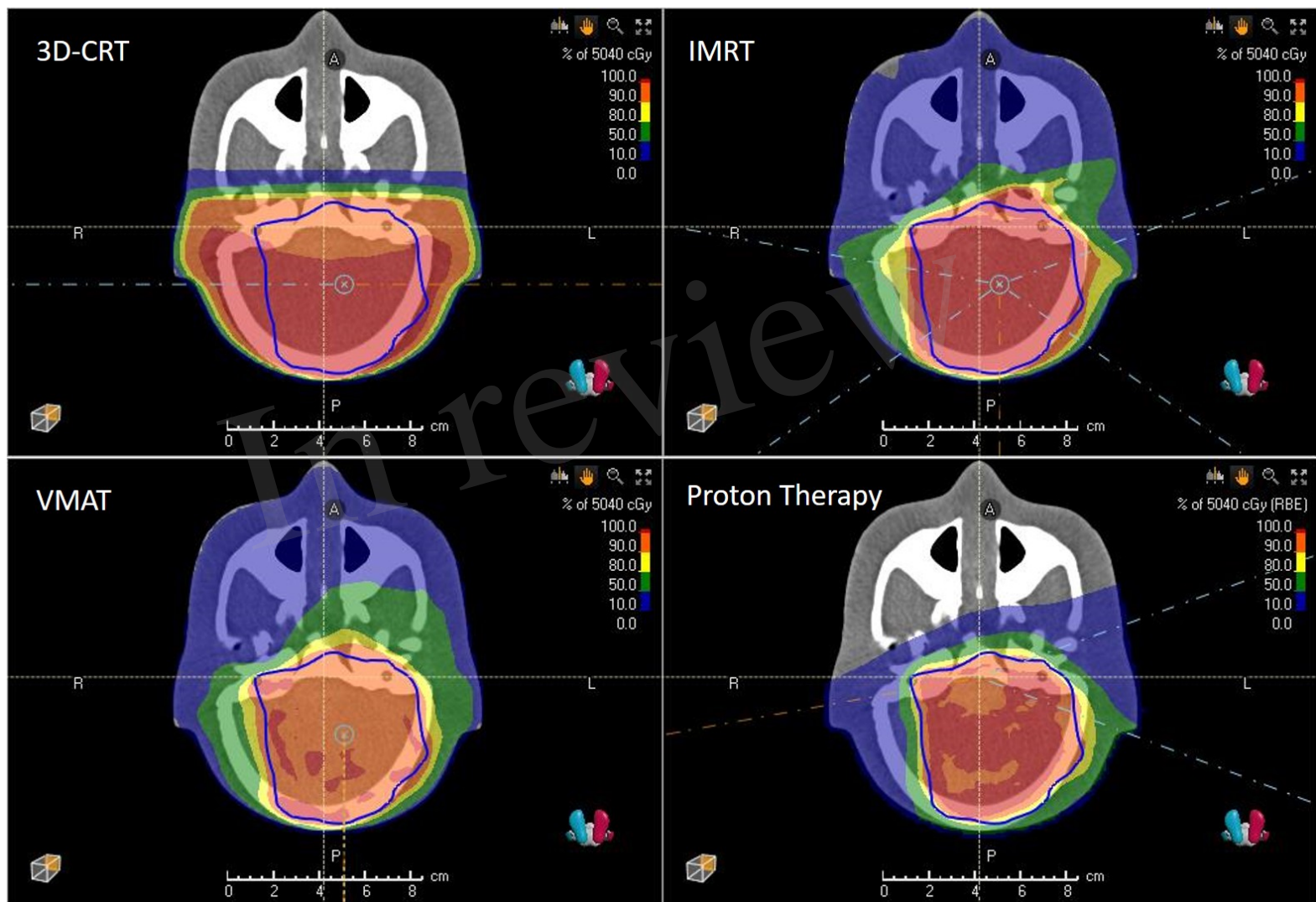


Figure 10.JPEG

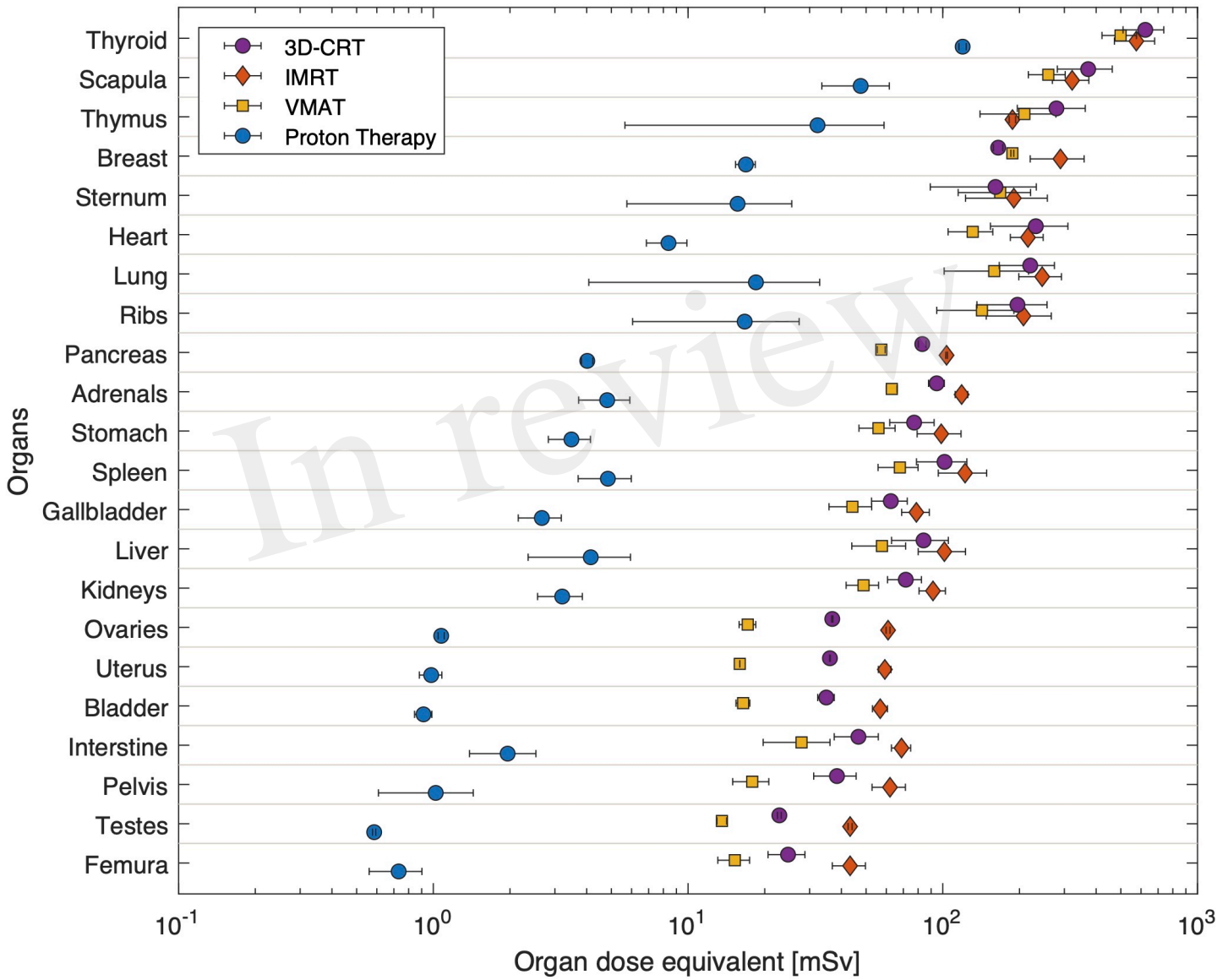


Figure 11.JPEG

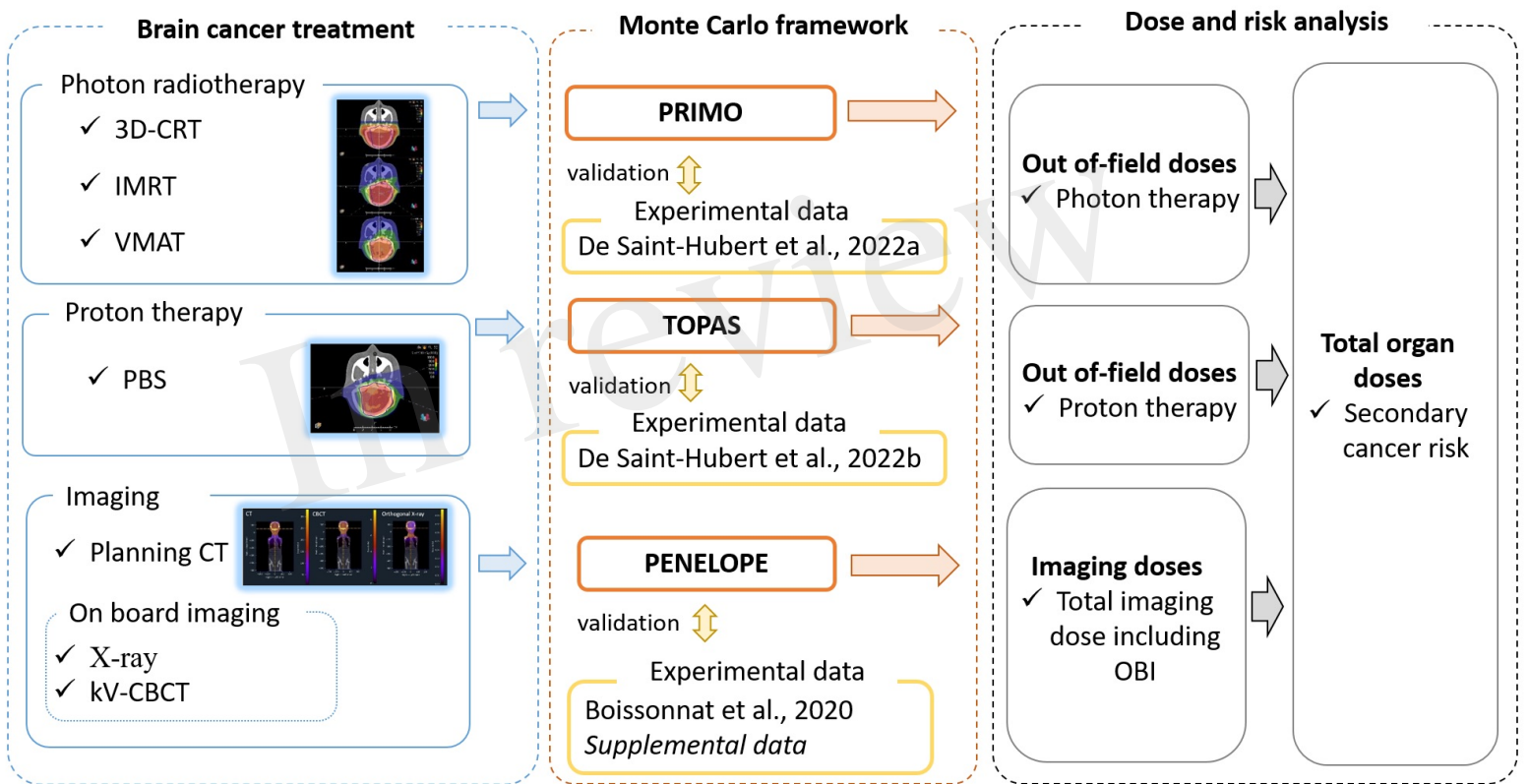


Figure 12.JPEG

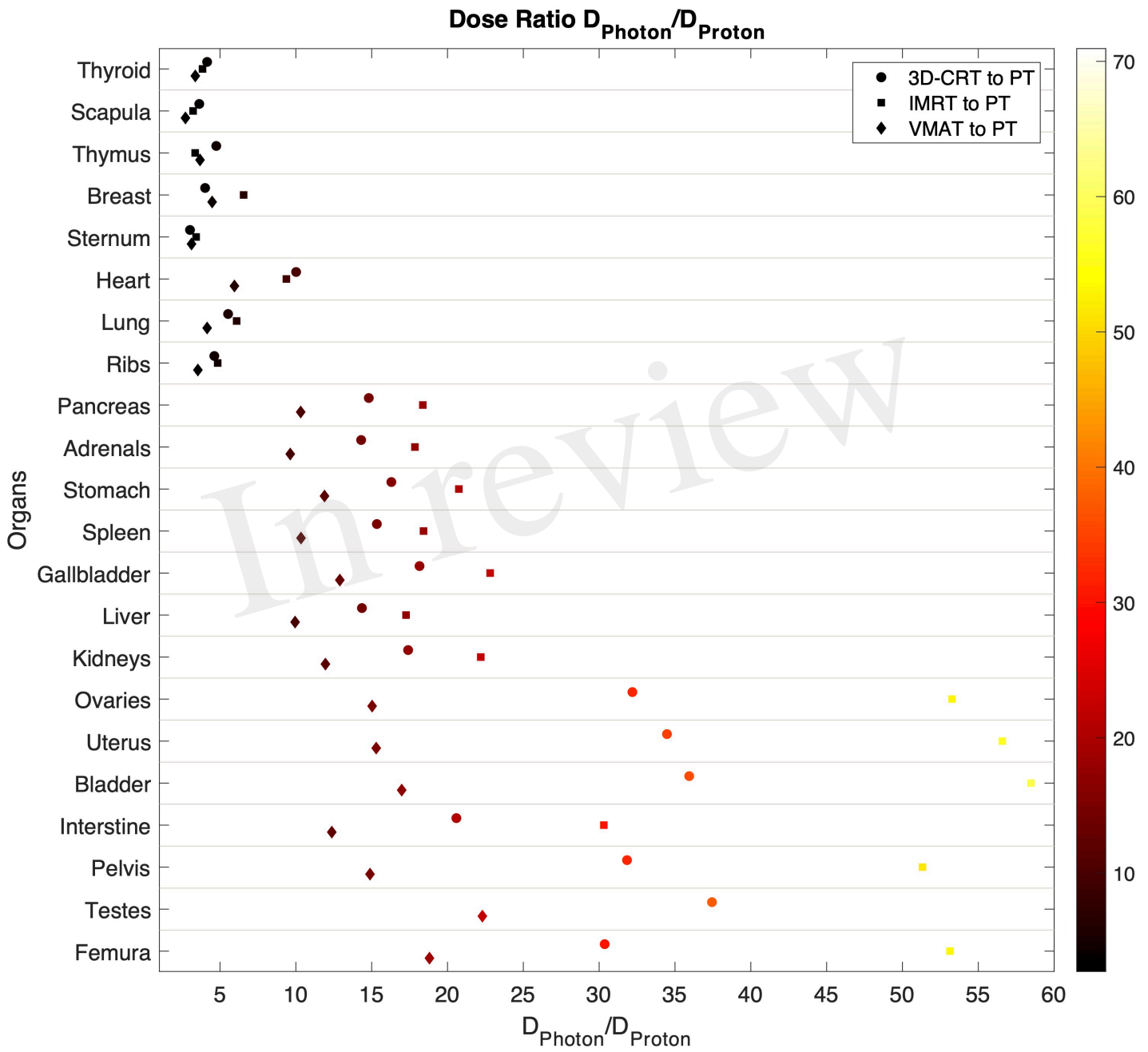


Figure 13.JPEG

